Heliyon 9 (2023) e18754

Contents lists available at ScienceDirect

Heliyon

journal homepage: www.cell.com/heliyon

Some aspects of the life of SARS-CoV-2 ORF3a protein in mammalian cells

Song Jiao [a,*,1,##], Pablo Miranda [a,**,1], Yan Li [b], Dragan Maric [c], Miguel Holmgren [a]

[a] Molecular Neurophysiology Section, National Institute of Neurological Disorders and Stroke, National Institutes of Health, Maryland, MD, USA
[b] Proteomics Core Facility, National Institute of Neurological Disorders and Stroke, National Institutes of Health, Maryland, MD, USA
[c] Flow and Imaging Cytometry Core Facility, National Institute of Neurological Disorders and Stroke, National Institutes of Health, Maryland, MD, USA

ARTICLE INFO

Keywords:
Stoichiometry
Viroporin
Cell death
Proximity labeling
Viral-host interactome
Mitochondrial fragmentation

ABSTRACT

The accessory protein ORF3a, from SARS-CoV-2, plays a critical role in viral infection and pathogenesis. Here, we characterized ORF3a assembly, ion channel activity, subcellular localization, and interactome. At the plasma membrane, ORF3a exists mostly as monomers and dimers, which do not alter the native cell membrane conductance, suggesting that ORF3a does not function as a viroporin at the cell surface. As a membrane protein, ORF3a is synthesized at the ER and sorted via a canonical route. ORF3a overexpression induced an approximately 25% increase in cell death. By developing an APEX2-based proximity labeling assay, we uncovered proteins proximal to ORF3a, suggesting that ORF3a recruits some host proteins to weaken the cell. In addition, it exposed a set of mitochondria related proteins that triggered mitochondrial fission. Overall, this work can be an important instrument in understanding the role of ORF3a in the virus pathogenicity and searching for potential therapeutic treatments for COVID-19.

1. Introduction

The COVID-19 pandemic caused by severe acute respiratory syndrome coronavirus 2 (SARS-CoV-2) constituted a serious threat to global human health and underscored the need of detailed research into this virus. SARS-CoV-2 has high sequence similarity to SARS-CoV and bat-borne coronaviruses, encoding four structural proteins, sixteen non-structural proteins and nine accessory proteins for viral replication and release [1,2]. Among the accessory proteins in SARS-CoV-2, ORF3a is the largest. It is an integral membrane protein with a unique structure, present exclusively in SARS-like coronaviruses. SARS-CoV-2 ORF3a exhibits a high sequence identity (73%) with its SARS-CoV homolog, particularly in functional domains, such as the three transmembrane (TM) regions, implying functional similarity among the homologous ORF3a proteins [3].

In this study, we have focused on four aspects of the biology of ORF3a: 1) its oligomerization state in mammalian cells, 2) its functional properties as an ion channel, 3) its localization within the infected cells, and 4) its proteomic vicinity, which unexpectedly led us to assess mitochondria dynamics.

* Corresponding author.
** Corresponding author.
E-mail addresses: jiaos@mail.nih.gov (S. Jiao), pablo.mirandafernandez2@nih.gov (P. Miranda).
[1] These authors contributed equally.
Lead contact.

https://doi.org/10.1016/j.heliyon.2023.e18754
Received 24 January 2023; Received in revised form 24 July 2023; Accepted 26 July 2023
Available online 1 August 2023

Cryo-electron microscopy studies have shown that ORF3a assembles as dimers or tetramers when over expressed in insect cells [4]. Biochemically, SARS-CoV ORF3a also appears to form dimers and tetramers [5]. It is thought that multiple intermolecular disulfide bridges in the cysteine-rich regions facilitate the formation of dimers and multiple non-covalent interactions between dimers form tetrameric complexes [5]. Nevertheless, the stoichiometry of SARS-CoV-2 ORF3a complexes in the mammalian host cells remains poorly understood. In this study, we assessed the native multimeric composition of ORF3a proteins by employing the perfluoro-octanoic acid (PFO)-PAGE method, which allows the analysis of multimeric complexes in a non-denaturing environment, thereby preserving protein-protein interactions [6]. Combining this approach with cell surface biotinylation strategies, we determined that the majority of ORF3a protein at the surface of cells are monomers and dimers.

Both SARS-CoV and SARS-CoV-2 ORF3a have been considered as putative viroporins. Potassium currents carried by SARS-CoV ORF3a have been reported in HEK293 cells and in Xenopus oocytes [5,7,8]. In addition, in the recent cryo-EM study, purified SARS-CoV-2 ORF3a dimers were incorporated into liposomes for electrophysiological characterization [4]. Clearly, these proteoliposomes exhibited robust ionic currents carried by non-selective cation channels [4]. We were unsuccessful in obtaining electrophysiological recording consistent with the cell surface expression of SARS-CoV-2 ORF3a in both HEK293 cells and Xenopus oocytes expression systems. Similar results were obtained with the *N*-terminus deletion mutant (ORF3ΔN), even though this construct had a robust cell surface expression.

In host cells, ORF3a protein is found in various organelles, including ER, Golgi, endosomes, lysosomes, and perinuclear regions [9,10]. The subcellular distribution of ORF3a is influenced by specific motifs, such as the tyrosine-based sorting YXXΦ motif and the diacidic (S/EGD) motif [11,12]. Consequently, ORF3a is involved in diverse biological processes in host cells. For instance, ORF3a residing on lysosomes inhibits the fusion between lysosomes and autophagosomes, protecting virus particles from degradation [13]. Lysosomal ORF3a may potentially deacidify lysosomes and inactivate lysosomal proteolytic enzymes, thereby promoting viral release through lysosomal exocytosis [14]. In this study, we focused on whether the expression pathway of ORF3a protein follows a similar expression pathway than a canonical pathway of membrane proteins. To track ORF3a expression in the cell, we co-transfected a fluorescently labeled version of SARS-CoV-2 ORF3a with different organelle markers. In general, we found that ORF3a protein is distributed among the ER, Golgi apparatus, lysosomes, and occasionally at the cell surface.

To further elucidate the molecular mechanisms underlying the biological roles of ORF3a, various approaches have been developed to determine which host proteins interact with ORF3a. Several studies have used the co-immunoprecipitation (Co-IP) method coupled with mass spectrometry analysis to examine the interactions between the SARS-CoV-2 ORF3a and host proteins in HEK293 cells and HeLa cells [13,15,16]. This traditional method tends to identify high affinity interactions. Thereby, transient or weak host proteins/ORF3a interactions are difficult to detect. An alternative approach, named proximity labeling, relies on the proximity of the bait protein fused to a biotinylation enzyme with the subcellular proteome or interactome at the time proteins are labeled [17]. The added advantage of this approach is that it can be performed in living cells. The proximity-dependent biotin identification method has been implemented in recent studies to profile the viral-host interactomes for SARS-CoV-2 [18–20]. Here we employed a proximity labeling method that incorporates a chemical inducible dimerization system consisting of FKBP and FRB proteins to conditionally anchor the biotinylation enzyme, ascorbate peroxidase derivative APEX2, to ORF3a proteins [17,21–23]. This method improves specificity in the detection of ORF3a-host protein interactions, high spatial labeling resolution, and fast-labeling kinetics (less than 1 min) [17,23]. Combining this method with label-free quantitative mass spectrometry, we mapped ORF3a-host interactomes in HEK293 cells, providing biochemical insights into how SARS-CoV-2 ORF3a hijacks cellular functions, including mitochondria biology.

2. Materials and methods

2.1. Cell lines

HEK293 and COS7 cells were obtained from American Type Culture Collection (ATTC) and kept in our lab. Cells were cultured in Dulbecco's modified Eagle's medium (DMEM, Gibco) with 10% heat-inactivated fetal bovine serum (Gibco) at 37 ^{o}C with 5% CO_2. Cells for electrophysiological recording and immunostaining were cultured with 1% penicillin-streptomycin.

2.2. Plasmids and transfection

Mammalian expression vectors pCMV and pBacMam were generous gifts from Ms. Raymond Fields (Viral Production Core Facility, NINDS, NIH) and Dr. Eric Gouaux (Oregon Health & Science University), respectively. cDNA encoding SARS-CoV-2 ORF3a (Gene ID: 43740569) was synthesized by Epoch, and then cloned with a C-terminal tag of eGFP or mCherry or a N-terminal 6xHis tag into the pCMV vector through restriction sites BamHI and SalI. The N-terminal truncated ORF3a (41 N-terminal amino acids deleted) was generated by PCR using the full-length ORF3a as a template. cDNAs encoding Shaker potassium channel (Shaker) and mouse Kv1.1 potassium channel (mKv) were cloned into pCMV vector. cDNA encoding human BK channel subunit β2 (hBK-β) was cloned into pBacMam vector. cDNA encoding human BK channel alpha subunit was cloned into pcDNA3 vector. ER marker, mCitrine-ER-5 was a gift from Michael Davison (Addgene plasmid #56557), Golgi marker mApple-Sit-N-15 was a gift from Michael Davison (Addgene plasmid #54948) and lysosome marker Lamp1-mTurquoise2 was a gift from Dorus Gabella (Addgene plasmid #98828) [24]. Plasmid mito-DsRed2 was a kind gift from Dr. Richard Youle, NINDS, NIH. Plasmid For proximity labeling, cDNAs encoding APEX2-FRB-mCherry, ORF3a-2xFKBP-eGFP and ORF3aΔN-2xFKBP-eGFP were cloned into pBacMam vector. Lipofectamine 3000 reagent was used for transfection on cultured cells.

2.3. Evaluation of ORF3a localization among subcellular fractions

A previously established method [25] was modified and utilized to isolate cytosolic fraction and membrane fraction of HEK293 cells. Briefly, HEK293 cells were rinsed and harvested with ice-cold PBS buffer, and then centrifuged at 3,000 × g for 10 min at 4 °C. Cell pellets were resuspended and incubated with Digitonin lysis buffer (PBS containing 45 μg/mL Digitonin and Roche cOmplete™ protease inhibitor cocktail) for 10 min at 4 °C under agitation, and then centrifuged at 15,000 × g for 10 min at 4 °C. The supernatant was collected as the cytosolic fraction, containing cytosolic proteins. The pellet was further lysed in NP-40 lysis buffer (PBS containing 1% NP-40 and protease inhibitor cocktail) for 20 min at 4 °C under agitation. Pellet lysate was centrifuged at 10,000 × g for 5 min at 4 °C and the resulting supernatant was collected as the membrane fraction, contains proteins from plasma membrane and membrane-bound organelles. Proteins in each fraction from different samples were analyzed and quantitated by SDS-PAGE for detecting the expression of target proteins. Membrane fraction lysates were subjected to PFO-PAGE to study the stoichiometry of ORF3a complex.

2.4. Assessment of surface ORF3a expression and stoichiometry

The plasma membrane of transfected HEK293 cells were biotinylated. Briefly, cells were rinsed with ice-cold DPBS buffer (PBS containing 2.5 mM $CaCl_2$ and 1 mM $MgCl_2$) three times and then incubated with 0.5 mg/mL Sulfo-NHS-biotin (Thermo Fisher) in DPBS buffer for 30 min at 4 °C. HEK293 cells were further washed three times with the quenching solution (50 mM Glycine in DPBS buffer) to stop the biotinylation, followed by another wash with PBS solution. Cells were subsequently harvested and pelleted by centrifugation (3,000 × g for 10 min at 4 °C). Cell pellets were lysed in NP-40 lysis buffer (PBS containing 1% NP-40 and protease inhibitor cocktail) for 20 min at 4 °C under agitation, and then centrifugated at 10,000 × g for 5 min at 4 °C to collect the supernatant.

To isolate biotinylated surface proteins from the supernatant, the supernatant was incubated with the monomeric avidin resin (CAT#20228, Thermo Fisher) prepared as per the instruction from the manufacturer. The permeant was collected as the Unbound sample, which contained proteins not biotinylated. A mild competitive elution with free biotin was implemented to dissociate biotinylated surface proteins from the avidin resin, to preserve the native structure of ORF3a oligomers. Briefly, resin was rinsed six times with NP-40 lysis buffer and incubated with biotin elution buffer (PBS containing 2 mM Biotin and 1% NP-40) for 10 min at 4 °C. The permeant was collected as the E1 sample, which contained biotinylated surface proteins. To assess the remaining biotinylated proteins bound to the resin after first elution, the resin was further incubated with a buffer containing 100 mM Glycine in H_2O at pH 2.5 for 10 min at 4 °C. The resulting permeant was collected as E2 sample. These proteins are likely denatured by the strong acidic environment.

The expression of ORF3a variants and Shaker-eGFP in the Unbound, E1 and E2 samples were analyzed and quantitated by SDS-PAGE. The elution sample E1 was also analyzed by PFO-PAGE to examine the stoichiometry of ORF3a at the cell surface.

2.5. PFO-PAGE for subunit stoichiometry analysis

The perfluoro-octanoic acid (PFO)-polyacrylamide gel electrophoresis (PAGE) is a validated method for assessing protein stoichiometry [6]. Briefly, membrane fraction lysates or purified protein samples were mixed 1:1 with PFO sample buffer (1–8% (wt/vol) NaPFO, 100 mM Tris, 20% (vol/vol) glycerol, and 0.005% (wt/vol) bromphenol blue, pH 8.0) and incubated under room temperature for 25 min. The samples were analyzed via gel electrophoresis using a PFO running buffer (25 mM Tris, 192 mM glycine, 0.5% NaPFO, pH 8.5, adjusted with NaOH) precooled to 4 °C. Once the running was complete, gels were soaked in 25 mM Tris buffer (pH 8.0) containing 0.05% (wt/vol) SDS for 5 min under room temperature, and then were subjected to electrophoretic transfer with a transfer buffer containing 25 mM Tris, 192 mM glycine and 20% (v/v) methanol. Immunoblotting was done using a standard protocol.

2.6. Electrophysiology

ORF3a and ORF3aΔN mRNAs were synthesized using T7 transcription kit (Thermo Fisher). 5 to 50 ng of mRNA was microinjected in *Xenopus laevis* oocytes (Ecocyte). Control oocytes were injected with water. Ionic currents were measured after 24 to 72 hours after injection using the two electrodes voltage clamp technique with an Oocyte Clamp OC-725C (Warner Instruments). For the recording, oocytes were kept in ND96 solution as the external solution (in mM: 96 NaCl, 2 KCl, 1.8 $CaCl_2$, 5 HEPES, pH 7.4) and 100 ms pulses were applied in 10 mV steps from -160 to 100 mV at a holding potential of 0 mV. High potassium solution (in mM: 98 KCl, 1.8 $CaCl_2$, 5 HEPES, pH 7.4) or NMDG solution (in mM: 100 NMDG, 5 HEPES, pH 7.6) were used instead of ND96 in some experiments.

Transfection of HEK293 cells with pCMV-ORF3a-GFP or pCMV-ORF3aΔN-GFP DNA was done using Lipofectamine 3000 (Thermo Fisher). Fluorescence expression was visually checked 24 hours after transfection, and fluorescence positive cells were used for patch clamp in 'whole cell' or 'inside out' excised patch configuration with an Axopatch 200B amplifier and Clampex software (pCLAMP 10, Molecular Devices). In 'whole cell' configuration, cells were maintained in physiological external solution (in mM: 140 NaCl, 4 KCl, 2 $CaCl_2$, 1 $MgCl_2$, 10 HEPES, pH 7.4), and the seal was made with Borosilicate glass pipettes (Harvard apparatus) with a resistance of 4–5 MΩ and an internal pipette solution (in mM: 140 KCl, 2 NaCl, 10 EGTA, 10 HEPES, pH7.4). In 'inside-out' configuration, a symmetric potassium solution was used inside and outside of the pipette (in mM: 130 KMES, 10 KCl, 10 EGTA, 10 HEPES, pH 7.4).

For single channel recording, borosilicate pipettes with a resistance of 5-8 MΩ were used. Membrane patches were excised, and a gap free protocol at a holding potential of 100 mV was recorded for 5 min. For the events quantification, random 25-second regions were selected, and a histogram of the events was obtained after adjustment of the baseline in Clampfit software (pCLAMP 10, Molecular devices).

2.7. Cell death assessment using flow cytometry

24 hours or 48 hours after transfection, HEK293 cells were incubated with 50 nM SYTOX Green nucleic acid stain (CAT#S7020, Thermo Fisher) and 1 μg/mL Hoechst 33342 (CAT#62249, Thermo Fisher) for 30 min at 37 °C, to mark the nuclei of dead cells and the nuclei of all cells, respectively. Cells were next washed in PBS solution and harvested by trypsinization. After washing, cells were resuspended in PBS solution and subjected to flow cytometry analysis for forward scatter area (FSC-A) as a reliable proxy for cell size, and fluorescence intensities, including mCherry, SYTOX staining, and Hoechst staining, for characterizing cells.

2.8. Immunoblot analysis

Immunoblotting was done using standard protocol. Mouse anti GFP antibody (CAT#MA5-15256, Thermo Fisher) was used to detect eGFP tagged Shaker proteins and ORF3a variant proteins in all the western blot assays. Donkey-anti-mouse HRP-conjugated secondary antibodies (CAT#711-035-151, Jackson ImmunoResearch) and ECL reagents (CAT#32109, Thermo Fisher) were used for protein detection by chemiluminescence.

2.9. APEX2-based proximity labeling in live cells

Plasmid encoding APEX2-FRB-mCherry was co-transfected with plasmid encoding ORF3a-2xFKBP-eGFP or ORF3aΔN-2xFKBP-eGFP at a molar ratio of 1:4 into HEK293 cells. To induce the heterodimerization between FRB and FKBP, 24 hours after transfection, HEK293 cells were incubated with 250 nM Rapalog (A/C Heterodimerizer, CAT#635056, TaKaRa) for 10 hours in a 37 °C incubator.

Next, APEX2 mediated proximity labeling was induced using the method modified from a previous protocol [17]. In brief, cells were incubated with 500 μM Biotin-phenol (CAT#SML2135, Sigma-Aldrich) for 30 min in 37 °C incubator, followed by 1 min H_2O_2 treatment (1 mM, CAT#H1009, Sigma-Aldrich) under room temperature. Cells were washed twice with quencher solution (DPBS containing 10 mM sodium ascorbate, 5 mM Trolox and 10 mM sodium azide), twice with DPBS and once with quencher solution. Cells were pipetted off with quencher solution and pelleted by centrifugation at 3,000 × g for 10 min at 4 °C. Cell pellet was resuspended and incubated with Digitonin lysis buffer, which was comprised of 150 mM sodium chloride, 20 mM Tris (pH 7.5), 45 μg/mL Digitonin, 10 mM sodium ascorbate, 5 mM Trolox, 10 mM sodium azide, 1 mM PMSF and protease inhibitor cocktail, for 10 min at 4 °C under agitation. Cell lysate was centrifuged at 15,000 × g for 10 min at 4 °C, and the supernatant was collected as the cytosolic fraction. Next, the pellet was washed twice with Digitonin lysis buffer and subsequently lysed in Urea lysis buffer which contained 150 mM sodium chloride, 20 mM Tris (pH 7.5), 6.5 M Urea, 10 mM sodium ascorbate, 5 mM Trolox, 10 mM sodium azide, 1 mM PMSF and protease inhibitor cocktail, for 1 hour at 4 °C under agitation, to solubilize the membrane proteins. Pellet lysate was centrifugated at 12,000 × g for 5 min at 4 °C, and the resulting supernatant was collected as the membrane fraction.

The samples for cytosolic fractions and membrane fractions were mixed with Pierce™ streptavidin magnetic beads (CAT#88816, Thermo Fisher) and incubated for 1 hour at room temperature on a rotator. The magnetic beads were pelleted using a magnetic rack and subsequently washed twice with the corresponding lysis buffer, once with 1 M KCl, once with 0.1 M sodium carbonate, once with 2 M urea in 10 mM Tris-HCl solution (pH 7.5), and twice with corresponding lysis buffer. All buffers were kept on ice during the procedure. The beads were further boiled in 2X SDS sample buffer to elute biotinylated proteins. The eluates were loaded onto the precast Novex Tris-Glycine gels and run for 0.5 cm. Gels were stained with EZBlue™ gel staining reagent and analyzed by liquid chromatography with tandem MS (LC/MS/MS).

2.10. Mass Spectrometry Analysis

In-gel samples (~5 μg per sample) were reduced using 10 mM Tris(2-carboxyethyl) phosphine hydrochloride at room temperature for 1hr and alkylated with 10 mM N-Ethylmaleimide for 10 min. Samples were digested with trypsin (Promega) at 37 °C overnight. The trypsin:sample ratio is 1:20 (w/w). After the extraction, peptides were cleaned with an Oasis HLB μElution plate (Waters). For LC-MS/MS experiment, an ES902 column (Thermo Fisher) was used to separate the peptides at a flowrate of 300nl/min. Mobile phase B (0.1% formic acid in ACN) amount was increased from 3% to 24% in 66 min, from 24% to 36% in 8 min, then followed by wash steps. Mobile phase A composition is 0.1% formic acid in H_2O. The MS1 scans were performed in orbitrap with a resolution of 120K. The mass range is 400-1500 m/z, and the AGC target is 4 x 105. The quadrupole isolation window is 1.6 m/z. The precursor ion intensity threshold to trigger the MS/MS scan was set at 1 x 104. The MS2 scans were acquired in ion trap in data-dependent mode. CID fragmentation method was used, and the collision energy was fixed at 30%. MS1 scan was performed every 3 sec. As many MS2 scans were acquired within the MS1 scan cycle.

Proteome Discoverer software version 2.4 was used for protein identification and quantitation. Raw data were searched against Sprot Human database. Maximum missed cleavage site was set to 1. Oxi(M) and NEM(C) was set as dynamic and fixed modification, respectively. Mass tolerances for MS1 and MS2 scans were set to 5 ppm and 0.6 Da, respectively. Percolator was used for PSM validation. The search results were filtered by a false discovery rate of 1% at the protein level. For each sample, protein abundance values were calculated for all proteins identified by summing the abundance of unique peptides matched to that protein. Each sample group contains 6 replicates. The normalization was performed against the total peptide amount. Protein ratios were calculated by comparing the median protein abundances between 2 conditions. ANOVA method was used for hypothesis test.

2.11. Gene ontology analysis

Gene ontology (GO) term analyses were produced using ShinyGo software package v0.76 (available from http://bioinformatics.sdstate.edu/go/ [26], PANTHER software version 17.0 (available from http://www.pantherdb.org/ [27], and ClueGO/CluePedia plugin [28,29] in Cytoscape software version 3.9.1 [30]. When comparing protein abundance in ORF3a or ORF3aΔN samples to those in the Control, proteins with p values less than 0.05 and positive log2 (fold-change) values were classified as the most significant interactors proximal to ORF3a (or ORF3aΔN).

The symbol lists of proximal proteins were analyzed using ShinyGo and PANTHER to identify cellular components enriched with ORF3a or ORF3aΔN interactomes. In ShinyGo software package v0.76, the p-value cutoff for gene clusters was set at FDR < 0.05 by default. Hierarchical clustering trees for significant biological processes were conducted by the software, in accordance with the enrichment FDR values of protein sets. Smaller FDR values indicated the higher confidence levels of the biological processes represented by the proximal proteins. The overrepresentation test using PANTHER software was conducted, using Fisher's exact test and the false discovery rate (FDR) for the calculation of the statistical significance and the correction of multiple tests, respectively. Homo sapiens data was used as the reference list using official gene symbol.

Functional enrichment analysis was performed in Cytoscape software with the ClueGO (version 2.5.9, [28]) and (CluePedia version 1.5.9 [29]) plugins, generating GO annotation networks for biological process and pathway terms. The P-value for enrichment significance was calculated by two-sided hypergeometric tests and adjusted with Bonferroni step-down method for multiple test correction. GO terms with a P-value less than 0.05 were considered significant. Kappa scores were further calculated to define the strength of connections between selected GO terms. The network was generated using yFiles Layout Algorithms [31] in Cytoscape app.

2.12. Immunostaining and imaging

Cells for imaging were grown on coverslips in 6-well plates. Transfected HEK293 cells were fixed and stained using a standard procedure. Cy5-conjugated streptavidin (1:4,000, CAT#016-170-084, Jackson ImmunoResearch) was utilized to detect biotinylated proteins. Cells were additionally stained by DAPI to visualize nuclei. Images were obtained using a Zeiss LSM 510 microscope system.

2.13. Live imaging

Live imaging was performed in COS7 cells grown in glass bottom 35mm dishes (MatTek). Cells were transfected with Lipofectamine 3000 to express fluorescent proteins, either in combination or alone. Endoplasmic reticulum was marked with mCitrine-ER-5. Golgi apparatus was marked with mApple-Sit-N-15. Lysosomes were marked with Lamp1-mTurquoise2. Mitochondria were labelled with mito-DsRed2, a gift from Dr. Richard Youle, NINDS, NIH. The marker plasmid and the fluorescently labeled ORF3a variants were transfected with Lipofectamine 3000 following manufacturer's instructions. A range of 100 ng to 1 ug of each plasmid was used. The amount of DNA transfected and excitation settings were adjusted to obtain a similar intensity for each fluorophore.

For image acquisition and linear unmixing, images were acquired on a Zeiss LSM 880 Spectral Confocal microscope equipped with a 32-channel GaASP spectral detector using a 63x/1.4 NA objective lens. The microscope was equipped with a heating stage and incubation system to maintain the cells at 37°C and 5% CO_2. All fluorophores were excited simultaneously using 405, 488 and 594 (or 405, 488 and 564) and the spectra was collected for each pixel in lambda mode at 9 nm bins from 415 to 690 nm. Spectra were defined for each fluorophore using images from cells transfected only with that fluorophore. Images from cells expressing all the fluorophores in similar intensity were used for linear unmixing with Zen Software (Zeiss). Images were obtained at 4, 12, 16 and 24 h after transfection, while maintaining the cells at 37°C and 5% CO2. For the experiments on mitochondrial fragmentation, the images were obtained at 24, 48 and 72 hours after transfection.

2.14. Mitochondrial size quantification

In cells co-expressing mito-DsRed2 and ORF3a variants labelled with GFP, images were obtained in the LSM 880 spectral microscope. Emission channel after excitation at 561 nm was used to determine mitochondrial expression. The images with DsRed2 fluorescence were used to analysis with custom-made codes for Matlab/Octave software to determine the size of the mitochondria. Briefly, the image was converted in a binary image, and the bwareaopen and bwconncomp functions were used to define the different mitochondria fragments. Using the regionprops function the area in pixels of each mitochondria fragment was measured. For each analyzed condition, at least 1500 individual mitochondria fragments were measured from different images obtained from the same plate. Histograms of the area distribution were created to compare between conditions.

2.15. Quantification and statistical analysis

Western blotting

Four biological replicates per sample were assayed.

Electrophysiology

Data were analyzed offline using Clampfit software (pCLAMP 10, Molecular devices). The single current events were counted within randomly selected 25-second regions from single channel recordings after the baseline adjustment. Sample size (n represents the number of *Xenopus* oocytes or HEK293 cells) was indicated in the corresponding figures. Error bars represent the SEM from

independent experiments.

Cell death assessment using flow cytometry

Eight biological replicates per sample were assayed. The p-values were calculated by a paired t test.

Mass spectrometry analysis

Six biological replicates per sample were assayed. The p-values were calculated by the ANOVA (Individual Proteins) method in the Proteome Discoverer software. Proteins were considered proximal to the bait protein (ORF3a or ORF3aΔN) if they had p values less than 0.05 and positive log2 (fold change) values.

GO terms

Determination of the enriched Gene Ontology (GO) terms was done in Cytoscape software with the ClueGO (version 2.5.9) and (CluePedia version 1.5.9) plugins. The calculation of p values was described in the Method section. P values less than 0.05 were used as a cutoff for significantly enriched GO terms.

Mitochondrial size quantification

The mitochondrial sizes were measured using custom-made codes for Matlab/Octave software for at least 1500 individual mitochondria fragments from different images per condition.

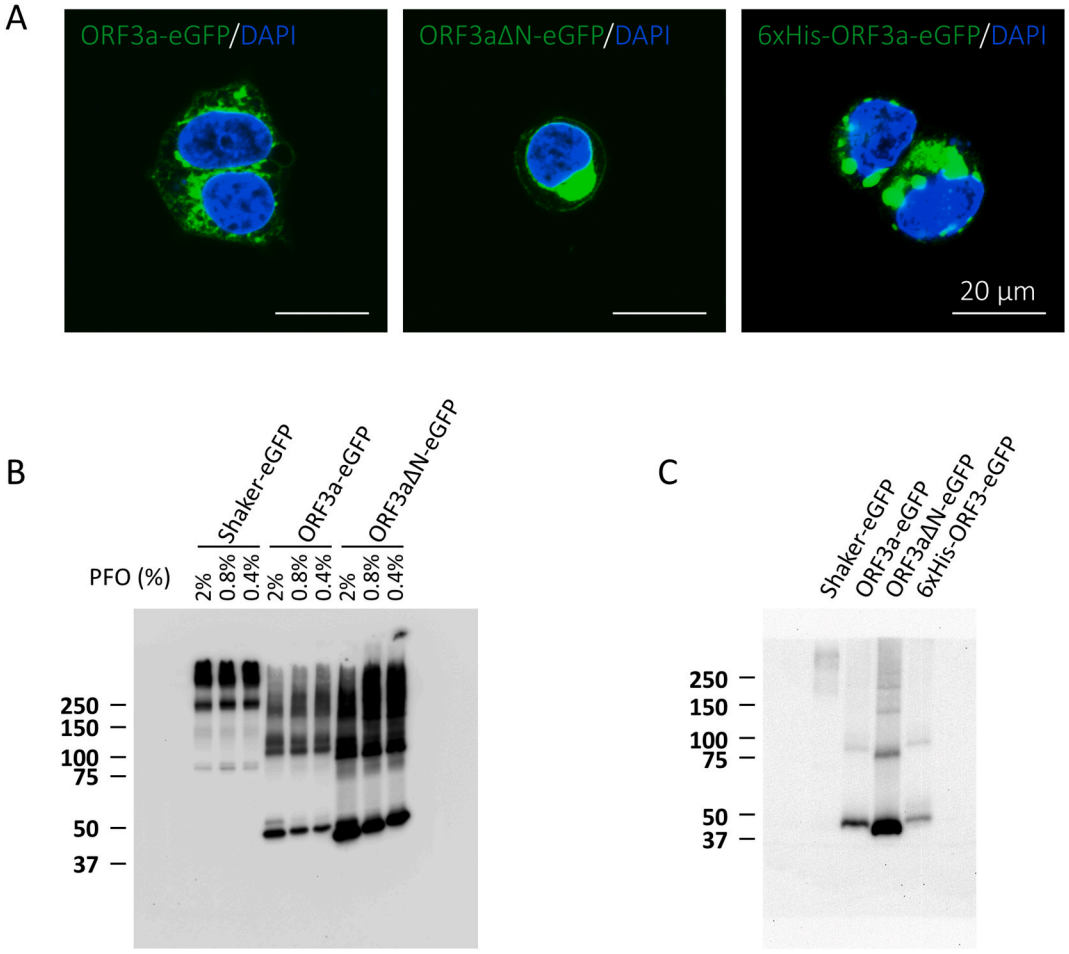

Fig. 1. Characterization of ORF3a variants in the HEK293 host cells. (A) Representative images of HEK293 cells transfected with different ORF3a variant constructs and stained with DAPI. Scale bar = 20 µm. (B) A representative blot for stoichiometry analysis of ORF3a variants in membrane fraction lysates using PFO-PAGE. The lysates were incubated with 2%, 0.8% and 0.4% NaPFO sample buffers. The original blot image can be found in the supplementary material, labeled as "Fig. 1B raw.png" (Fig. S1). (C) A representative blot for stoichiometry analysis of ORF3a variants on cell surface membrane using PFO-PAGE. The lysates were incubated with 1% NaPFO sample buffer. The original blot image can be found in the supplementary materia, labeled as "Fig. 1C raw.png" (Fig. S2).

3. Results

3.1. Stoichiometry and assembly of SARS-CoV-2 ORF3a in HEK293 cells

To examine the subunit stoichiometry of SARS-CoV-2 ORF3a, three different *C*-terminus eGFP fusion ORF3a variants were developed: full length (ORF3a-eGFP), *N*-terminus truncated (ORF3aΔN-eGFP) and *N*-terminus polyhistidine tagged (6xHis-ORF3a-eGFP), along with an eGFP-fused Shaker potassium channel protein, as control for assembling. First, we asked whether ORF3a variants are exclusively present in the membrane fraction of cell lysates. One day after transfection, HEK293 cells were lysed with digitonin to collect the cytosol fraction and then treated with NP-40 to obtain the membrane fraction. Not surprisingly, proteins from all the constructs were exclusively detected in the membrane fraction of cell lysates (Figure S1A), suggesting that their transmembrane segments were translated correctly by the ER.

Fig. 1A shows examples of HEK293 cells overexpressing ORF3a variants. In all three variants, the majority of ORF3a were observed within the subcellular membrane compartments. Only a small fraction of ORF3a were detected at the plasma membrane, more noticeable in the ORF3aΔN-eGFP variant, which is consistent with previous findings [4,5].

SARS-CoV-2 ORF3a appears to assemble as dimers and tetramers in heterologous expression systems [4,5]. To study the stoichiometry of ORF3a in a more native state, we implemented the PFO-PAGE method using the membrane fraction of HEK293 cells. To assess the effect of NaPFO on the assembly of our constructs, we tested three concentrations of NaPFO: 0.4, 1 and 2%. Shaker K^+ channels display a similar pattern of subunit assembling across all NaPFO concentrations (Fig. 1B), with a very small amount of monomers (~100 kDa band), a more prominent presence of dimers (~200 kDa band) and two large bands that represent tetrameric complexes of different stages of glycosylation, as described previously [32]. ORF3a-eGFP and ORF3aΔN-eGFP variants appear to be more abundant as monomers (Fig. 1B). On the contrary, Shaker complexes were not influenced by the NaPFO concentration, suggesting that the protein-protein interactions within ORF3a multimers were less stable than those of Shaker K^+ channels (Fig. 1B).

Next, we assessed which forms of ORF3a variants exist at the cell surface. We implemented a cell surface biotinylation approach, followed by the NaPFO-PAGE method (See Methods). Because ORF3a variants are mostly localized in intracellular organelles (Fig. 1A), they were predominantly detected in the Unbound samples (Fig. S1B), which contain the unbiotinylated proteins. Less amounts of ORF3a variants, particularly ORF3a and 6xHis-ORF3a, were detected in the E1 and E2 eluates, which contain the biotinylated proteins

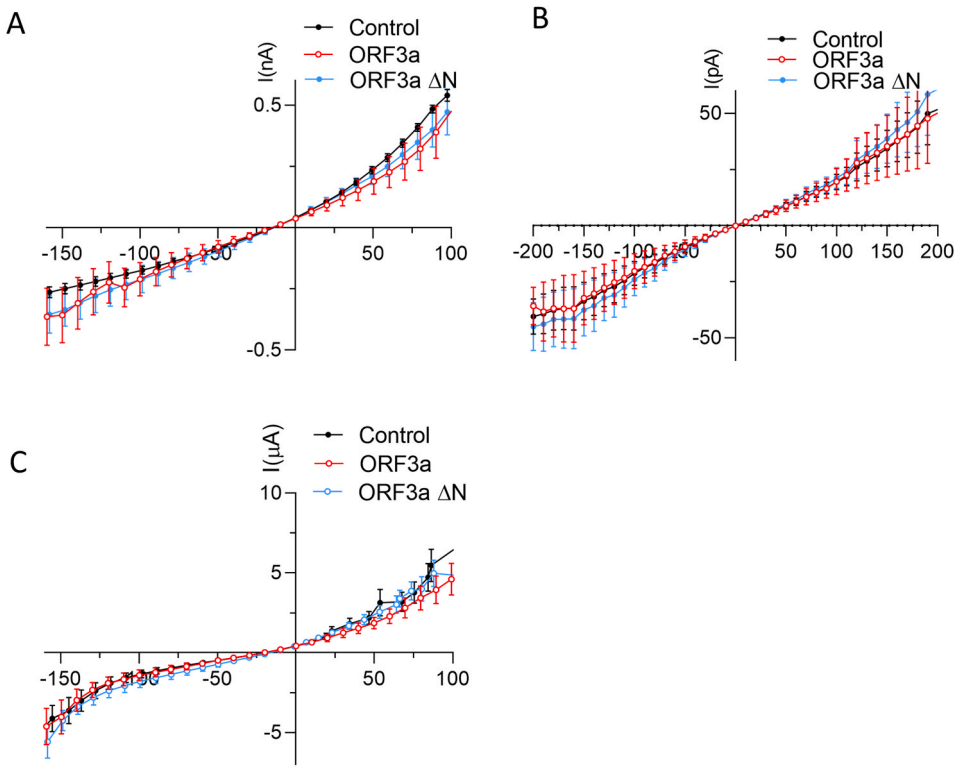

Fig. 2. Expression of ORF3a or ORF3aΔN in *Xenopus* oocytes or HEK293 cells does not produce detectable ionic currents. (A) I/V curves of whole cell currents recorded from HEK293 control cells (black, n = 5), cells expressing ORF3a (red, n = 5) and cells expressing ORF3aΔN (blue, n = 5). (B) I/V curves of inside-out patch currents recorded in symmetric K^+ from HEK293 control cells (black, n = 5), cells expressing ORF3a (red, n = 7) and cells expressing ORF3aΔN (blue, n = 4). (C) I/V curves of currents recorded using two-electrode voltage clamp in *Xenopus* oocytes injected with water (black, n = 5), oocytes injected with ORF3a cRNA (red, n = 7) and oocytes injected with ORF3aΔN cRNA (blue, n = 9). Error bars represent the S.E.M.

(Fig. S1B). Surprisingly, in all ORF3a variants, the prevalent form at the cell surface is the monomeric (Fig. 1C), followed by dimers. In the case of ORF3aΔN-eGFP variant, trimers and tetramers were also detected, yet at much lower levels (Fig. 1C). These results suggest that the multimeric assembling of ORF3a variants might not be a prerequisite for trafficking to the cell surface.

To further evaluate the assembling of ORF3a multimers in living cells, we co-transfected ORF3a variants with distinct fluorescence tags into HEK293 cells, and one day later inspected their subcellular localization based on fluorescence signals (Fig. S1C). When the same ORF3a variant fused with eGFP or mCherry were co-expressing in the same cell, eGFP and mCherry overlapped in all regions where the ORF3a variant was detected. In addition, the presence of both fluorescent tags in a cell did not change the subcellular location patterns observed when only one tag was transfected. Interestingly, when two constructs of ORF3a variants with distinct

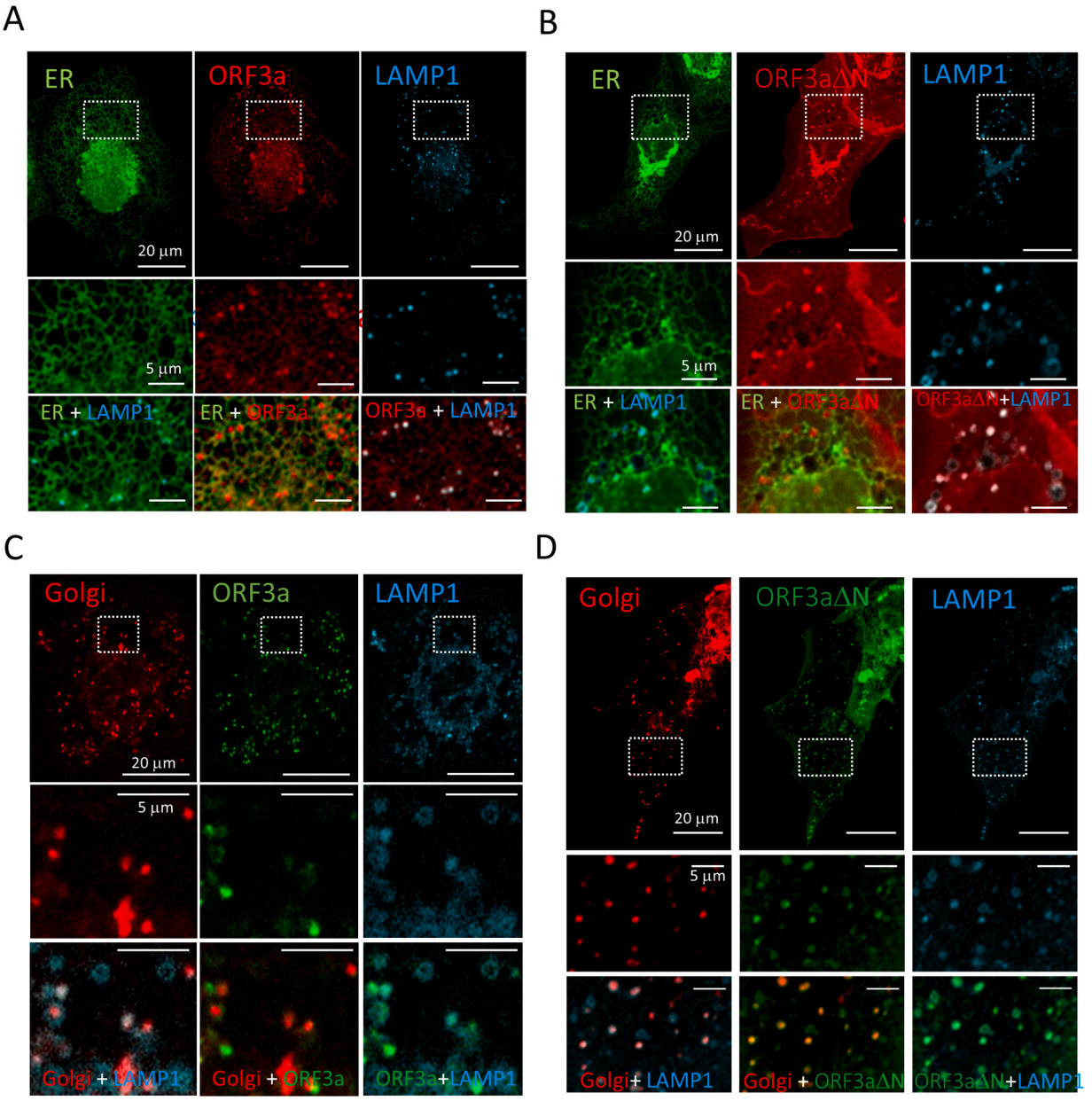

Fig. 3. Subcellular localization of ORF3a variants in mammalian cells. (A) A representative COS7 cell transfected with ORF3a-mCherry (*top middle panel*), ER marker (*top left panel*) and lysosome marker (*top right panel*). (B) A representative COS7 cell transfected with ORF3aΔN (*top middle panel*), ER marker (*top left panel*) and lysosome marker (*top right panel*). (C) A representative COS7 cell transfected with ORF3a (*top middle panel*), Golgi marker (*top left panel*) and lysosome marker (*top right panel*). (D) A representative COS7 cell transfected with ORF3aΔN (*top middle panel*), Golgi marker (*top left panel*) and lysosome marker. Middle-row panels show a magnification of the white square from top panels. Bottom row panels show the same magnified area with the combination of two channels for colocalization. Scale bars correspond to 20 μm in the full images or 5 μm in the inserts.

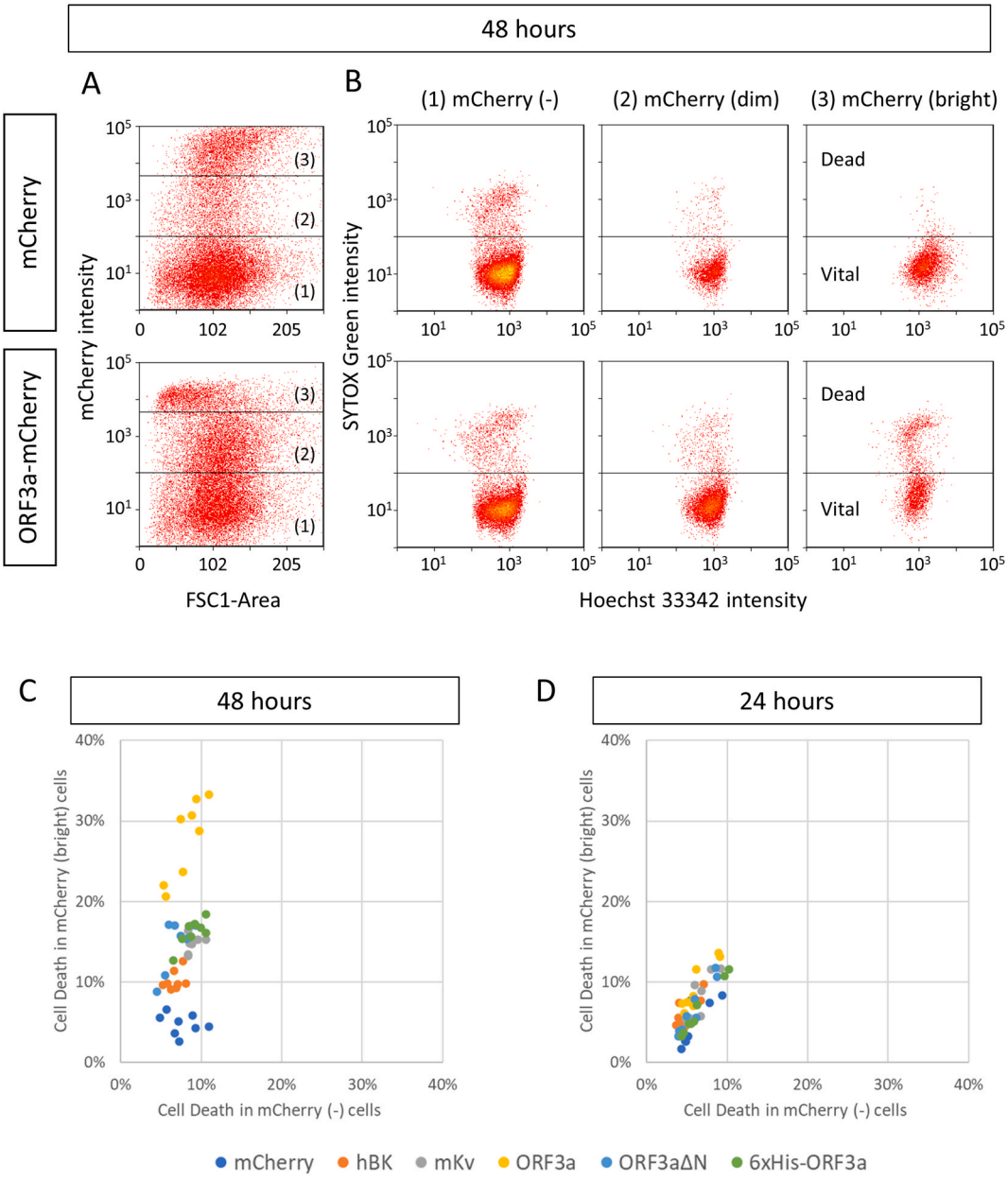

Fig. 4. Assessment of cell death induced by the expression of ORF3a variants. HEK293 cells were transfected with mCherry or mCherry tagged constructs and subsequently stained with Hoechst 33342 and SYTOX Green for flow cytometry analysis. (A) Representative density plots from flow cytometry analysis on HEK293 cells expressing mCherry or ORF3a-mCherry for 48 h. The x axis, FSC1-Area, represents relative cell size. Based on mCherry intensity, three cell populations were selected and labeled as (1), (2) and (3) for mCherry (−), mCherry (dim) and mCherry (bright) cells, respectively. The manual thresholds were placed at the top edge of the cell population for mCherry (−) cells and the bottom edge of the cell population for mCherry (bright) cells. These thresholds were kept constant in all samples. (B) Representative density plots of Hoechst *vs* SYTOX intensities for all three cell populations. The threshold separating vital and dead cells was manually selected above the edge the SYTOX Green negative cell population. It was kept constant for all samples. Dot colors in A and B reflect the density of local dots, and thereby yellow spots indicate a large number of detected cells. (C, D) Scatter plots for cell death rates of mCherry (bright) cells *vs* the cell death rates of mCherry (−) cells 48 h or 24 h after transfection, respectively. Each dot represents a single data point, while dot colors refer to the different constructs. Eight biological replicas from three independent experiments were obtained for each construct.

fluorescence labels were co-transfected into the same cells, the overlapping between eGFP and mCherry signals was incomplete, especially at the plasma membrane. As shown in Fig. S1C, the co-localization of 6xHis-ORF3a-mCherry and the co-expressed ORF3a-eGFP or ORF3aΔN-eGFP occurred in various subcellular regions, but not at the plasma membrane, where more ORF3a-eGFP or ORF3aΔN-eGFP than 6xHis-ORF3a-mCherry were detected. These results indicate that heterodimers, if formed at all, are not

efficiently targeted to the cell surface.

Can SARS-CoV-2 ORF3a or ORF3aΔN exhibit ion channel activity at the cell surface? Considering that we can detect expression at the cell membrane of fluorescent constructs of ORF3a and ORF3aΔN, we transfected their DNA into HEK293 cells. The expression of these variants was verified visually under the microscope and cells showing fluorescence were used in the whole cell or the inside-out excised patch clamp configurations to record macroscopic currents and single channel events. The whole cell recordings were made in presence of physiological external solution (in mM: 140 NaCl, 4 KCl, 2 $CaCl_2$, 10 HEPES, pH 7.4), with the expectation that cells expressing an ORF3a variant would show larger ionic currents than mock transfected cells. Fig. 2A illustrates the I/V curves obtained from cells expressing ORF3a, ORF3aΔN and control cells. No differences between the total membrane currents were observed at any of the voltages tested. We also performed experiments with excised patches from cells expressing ORF3a variants and control, recording the membrane currents in symmetric K^+ solutions. As shown in Fig. 2B, the I/V curves recorded in those conditions were not different. Additionally, single channel events were observed at voltages above 80 or below −80 mV in cells expressing ORF3a variants and controls, likely from native HEK293 ion channels (Fig. S2).

We proceeded to assess channel activity using the *Xenopus* oocyte expression system, in which viroporin activity by SARS-CoV had been previously reported [5]. We injected the cRNA encoding for ORF3a or ORF3aΔN and recorded the total membrane currents using the two electrodes voltage clamp technique. As control we used oocytes injected with water. Using standard ND96 media (in mM, 96 NaCL, 2 KCl, 1.8 $CaCl_2$, 5 HEPES), we were unable to reproduce the previously reported K^+ currents (Fig. 2C). Moreover, we tried external media with high potassium or replacing external monovalent cations with NMDG, finding no changes in ionic currents detected between the ORF3a constructs and the control (Fig. S3).

3.2. ORF3a trafficking across different subcellular compartments

Do SARS-CoV-2 ORF3a and ORF3aΔN variants follow canonical membrane protein trafficking paths? To approach this question, we monitored the trafficking of these proteins within subcellular organelles after transfection, using COS7 cells, instead of HEK293 cells, to have better spatial resolution. Cells were co-transfected with a combination of DNAs encoding for a specific ORF3a fluorescent variant and two additional constructs encoding for fluorescent markers of subcellular organelles. Fluorescence from ORF3a was observed in the ER, the Golgi, and, within 16 h, it could also be detected in lysosomes. As shown in Fig. S3, a small percentage of cells exhibited fluorescence at the plasma membrane as well. Fig. 3A shows representative images of a cell co-transfected with ER-citrine (Top left panel), ORF3a-mCherry (Top middle panel) and LAMP1-turquoise (Top right panel). The middle row panels correspond to magnifications indicated by a white square in the top panels, while the bottom row shows simultaneously the fluorescence of two of the imaging channels. From these images, it is evident that the ORF3a-mCherry colocalizes with the lysosome marker LAMP1-turquoise and the ER marker ER-citrine (Fig. 3A). Fig. 3C shows a representative cell co-transfected with the Golgi marker mApple-Sit-N-15, ORF3a-eGFP and LAMP1. Clearly, ORF3a colocalizes with both the Golgi and lysosome markers. Fig. 3B and D show representative images of cells co-transfected with ORF3aΔN, LAMP 1 and either the ER or the Golgi marker. Similarly, ORF3aΔN colocalize with LAMP1, ER and Golgi marker. In addition, ORF3aΔN was detected at the cell surface more frequently than ORF3a. Another noticeable difference is the presence of ORF3aΔN associated with large structures labeled with LAMP1 as we can see in Fig. 3D bottom row. These might represent the presence of ORF3aΔN in endosomes after internalization from the plasma membrane. Altogether, these results are consistent with these variants following a canonical membrane protein expression pathway, from ER to Golgi and plasma membrane. The strong presence of ORF3a in lysosomes agrees with previous reports on its function in lysosomal exocytosis as a way for viral release from the cell [33].

3.3. Time-dependent cell death of HEK293 cells induced by ORF3a

To investigate cell death induced by SARS-CoV-2 ORF3a protein, we transfected HEK293 cells with plasmids encoding mCherry alone or *C*-terminal mCherry fusion proteins including human BK channel β2 subunit (hBK-β2-mCherry), mouse Kv1.1 protein (mKv-mCherry), full length ORF3a (ORF3a-mCherry), ORF3aΔN-mCherry and 6xHis-ORF3a-mCherry. The mCherry, human BK channel β2 subunit and mouse Kv1.1 proteins were implemented as controls for cytosolic protein, transmembrane protein, and ion channel protein, respectively.

At 24 or 48 h after transfection, the expressions of transfected proteins were evaluated using fluorescence microscopy. We then harvested the cells and assessed cell death rates by flow cytometry using SYTOX Green, which labels dead cells and Hoechst 33342 to label all cells. Fig. 4 shows flow cytometry data from cells transfected with mCherry and ORF3a-mCherry. After the flow cytometry assay, cells were categorized into three groups based on the intracellular mCherry intensity: mCherry (−), mCherry (dim) and mCherry (bright) (Fig. 4A). Within each group, vital and dead cells were selected depending on the SYTOX Green intensity (Fig. 4B). The accompanying flow cytometry data for 48 h from the other constructs are shown in Figure S4A. Fig. 4C represents the percentage of cell death in the mCherry (−) group *vs* the percentage of cell death in the mCherry (bright) group for all constructs from 8 samples incubated for 48 h. Because overexpression of cytosolic mCherry alone did not induce cell death, the cell death percentage in both groups are similar (Fig. 4C, blue dots). Even though the overexpression of control membrane proteins led to higher cell death percentage than cytosolic mCherry, ORF3a-mCherry robustly induced cell death to values between 20% and almost 35% ($p = 7.60e\text{-}7$, for the comparison between ORF3a-mCherry (bright) cells and ORF3a-mCherry (dim) cells) (Fig. 4C, yellow dots). The flow cytometry data from one example incubated for 24 h after transfection is shown in Figure S4B. At 24 h, the changes in cell death percentages for all membrane proteins were smaller (Fig. 4D). The corresponding plots for the mCherry (dim) group reveal that the lower overexpression of any of the membrane protein constructs was not sufficient to induce cell death (Fig. S5 A & B).

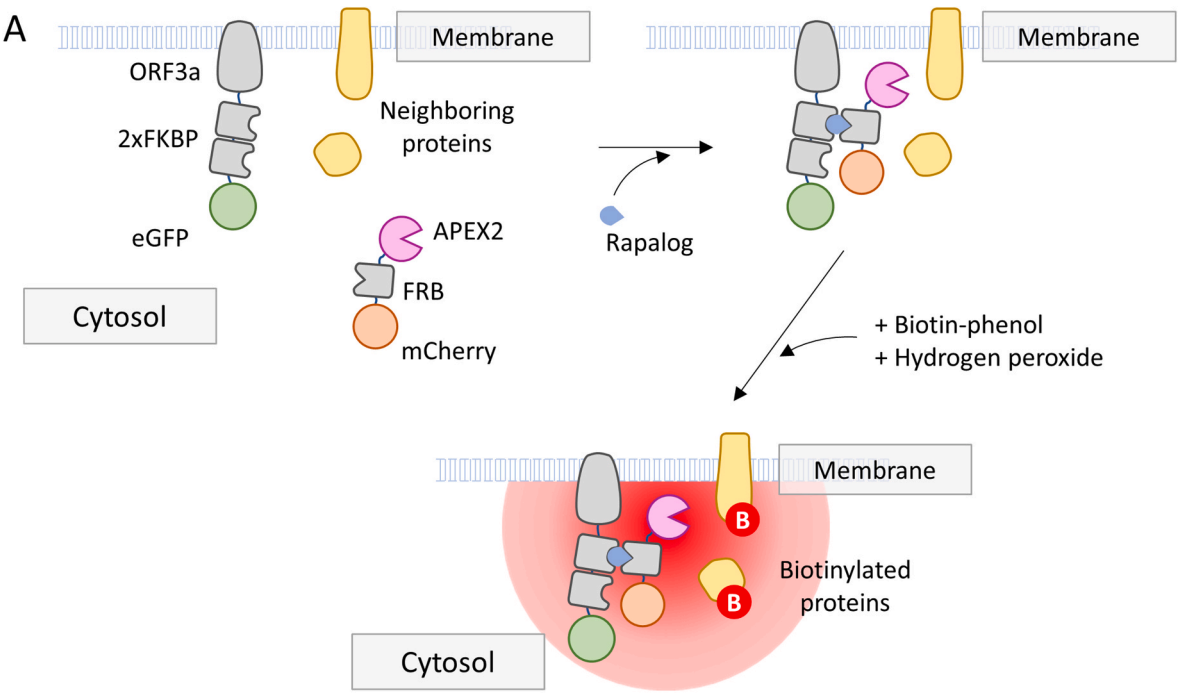

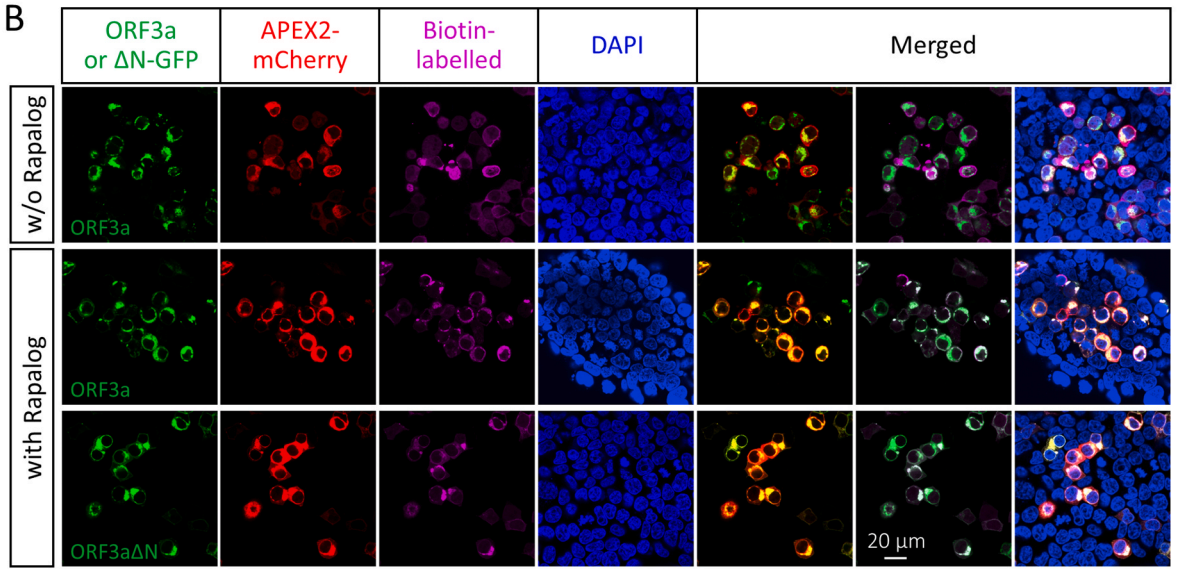

Fig. 5. ORF3a-host interactors using APEX2-dependent proximity labeling. (A) Cartoon showing the Rapalog-induced heterodimerization and APEX2-mediated biotinylation. Rapalog mediates dimerization between ORF3a-2xFKBP-eGFP and APEX2-FRB-mCherry, followed by biotin-phenol and H_2O_2 to initiate biotinylation. (B) Representative images of HEK293 cells expressing proximity labelling constructs. Cells were transfected with plasmids encoding for APEX2-FRB-mCherry and ORF3a-2xFKBP-eGFP or ORF3aΔN-2xFKBP-eGFP. Then, cells were incubated with or without Rapalog. Biotinylated proteins were visualized using streptavidin Cy5 conjugate. Merged images show the overlap between ORF3a (or ORF3aΔN) and APEX2 (*left*), ORF3a (or ORF3aΔN) and biotinylated proteins (*middle*), and all four channels (*right*). Scale bar = 20 μm.

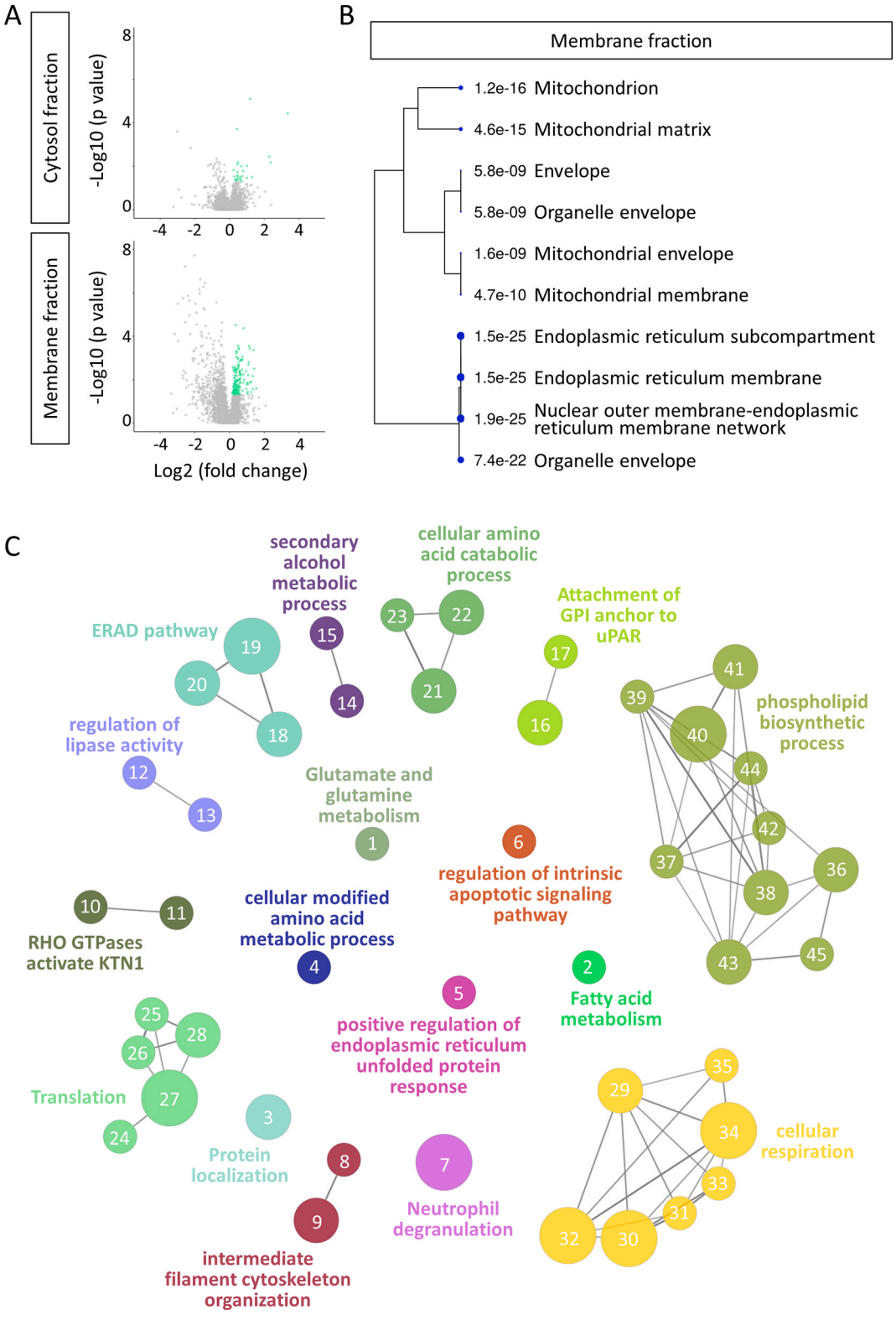

(caption on next page)

Fig. 6. ORF3a-host interactome. (A) Volcano plots showing changes in the abundance of biotinylated proteins between control and ORF3a in the cytosolic fractions (*top*) and the membrane fractions (*bottom*). The x axis represents the log2 (fold change), while the y axis represents the -log10 (P value). Proteins with positive log2 (fold change) values and p values less than 0.05 are highlighted in green. (B) Dendrogram illustrating the top ten over-represented GO cellular component terms in the proteins significantly interacting with ORF3a in the membrane fraction. The sizes of the blue dots correspond to the Enrichment FDR values (indicated next to each individual dot) for the GO cellular components obtained from ShinyGo software. (C) ClueGO networks depicting biological processes and pathways identified from ORF3a proximal proteins in both the cytosol and the membrane fractions. Circles (nodes) reflect GO terms for biological processes and pathways. Clustering is based on proteins shared between GO terms (nodes). The node sizes are proportional to the significance (adjusted P value) of each GO term. Numbers in nodes represent the row numbers from Table S3. Bold term labels represent the leading group terms (Table S3, ✓). The thickness of lines connecting GO terms represents the strength of the interaction.

Interestingly, the distribution of the cell sizes for the ORF3a-mCherry (bright) group at 48 h after transfection (Fig. 4A; bottom plot) is notoriously skewed towards the smaller end of the cells size axis. Cell shrinkage is a morphological outcome of cell death [34].

3.4. Interactome identification of ORF3a and ORF3aΔN variants using proximity labeling

To identify the proteins that interact with ORF3a when expressed in mammalian cells, we developed a proximity-based labeling method that exploited the APEX2-mediated biotinylation combined with a chemically inducible dimerization system. We utilized Rapalog-induced heterodimerization of FKBP and FRB proteins [22] to recruit APEX2 [23] to ORF3a or ORF3aΔN. In principle, APEX2 would biotinylate the proteins in the heterodimer vicinity upon supplementation with biotin-phenol and the oxidizing agent hydrogen peroxide (Fig. 5A).

Since *N*-terminus modifications affect the localization of ORF3a variants, we developed constructs that add two FKBP domains followed by eGFP at the *C*-termini of ORF3a and ORF3aΔN (Fig. 5A). FRB and mCherry were added to the *C*-terminus of APEX2 (Fig. 5A). APEX2-FRB-mCherry (4 μg) and ORF3a-2xFKBP-eGFP (16 μg) or ORF3aΔN-2xFKBP-eGFP (16 μg) were co-transfected in a T75 cm^2 flask in which HEK293 cells were cultured. The excess of DNA encoding the ORF3a variants ensured that most cells containing APEX2-FRB-mCherry also contain the bait. To promote the formation of FKBP-FRB heterodimers, we incubated the transfected cells with Rapalog for 10 h, which allowed an almost complete convergence of red and green fluorescence emitted from the APEX2 and ORF3a (or ORF3aΔN) fusion proteins, respectively (Fig. 5B). HEK293 cells expressing fluorescent APEX2 and ORF3a fusion proteins that were not treated with rapalog served as controls (Fig. 5B). Once proteins were biotinylated, they could be detected by immunostaining (Fig. 5B) or used for proteomic analysis. Biotinylation by APEX2 was clearly robust (Fig. 5B). In contrast, no biotinylated proteins were detected in the HEK293 cells that were treated only with biotin phenol, without hydrogen peroxide (Fig. S6A). Trace amount of biotinylation was observed in a few HEK293 cells when the treatment was made with hydrogen peroxide without supplementing biotin phenol (Fig. S6B), as previously reported [17]. The biotinylation caused by these traces of biotin is expected to have a negligible influence on the search for ORF3a interactors.

For mass spectrometry proteomic analysis, the biotinylated proteins were extracted from the membrane and cytosolic fractions using streptavidin magnetic beads (see Methods). HEK293 cells transfected with APEX2 and ORF3a fusion proteins that were not treated with Rapalog are referred as control, while those treated with Rapalog are denoted as ORF3a and ORF3aΔN. Six replicates were performed for both variants and the control. Here we will focus on the results for ORF3a, while an equivalent analysis for ORF3aΔN is displayed and discussed in Fig. S7. From the cytosolic fractions, 3251 biotinylated proteins were identified in the control and ORF3a samples (Table S1). From the membrane fractions, which included biotinylated proteins from both the plasma membrane and the subcellular organelles, 3096 biotinylated proteins were detected in the control and ORF3a samples (Table S1). Biotinylated proteins exhibited high variability in their abundances between the control and ORF3a samples, as depicted by the volcano plots (Fig. 6A). To identify the proteins proximal to ORF3a, representing those that have been concentrated in the ORF3a samples relative to the control samples, we implemented the criterium that the p-value between the test and control should be lower than 0.05. We identified 26 and 166 proteins proximal to ORF3a in the cytosolic and membrane fractions, respectively, highlighted in green (Fig. 6A, Table S1).

Because ORF3a is a membrane protein, the proximal proteins in the membrane fraction should reflect where ORF3a was located and its interactions with the organelles. We performed gene ontology (GO) enrichment analysis using ShinyGo software package to identify the organelles and protein ensembles associated with these proximal proteins. The top 10 over-represented GO terms are displayed in Fig. 6B. Consistent with our cell imaging study, many identified proximal proteins were from the endoplasmic reticulum (72 proteins) and the nuclear outer membrane-endoplasmic reticulum membrane network (60 proteins). We also identified 25 and 15 proteins associated with the Golgi apparatus and lysosomes, respectively, yet these organelles were not among the top ten GO terms.

Next, we conducted a GO enrichment analysis to determine the significant biological processes and pathways associated with the proximal proteins to ORF3a. This analysis was performed with ClueGO plugin [28] in Cytoscape [30]. We used the 192 proteins that were identified as proximal to ORF3a, with the human genome serving as the background reference. GO biological process and pathway terms were queried for enrichment. After implementing GO Term Fusion and discarding GO terms with Term P values larger than 0.05, we identified 45 GO terms that were associated with proximal proteins to ORF3a, which were represented by 17 leading GO Terms (Fig. 6C, Table S3). Interestingly, several of these biological processes are potentially relevant for viral infection and consistent with our previous observations. For example, the regulation of intrinsic apoptotic signaling pathway (GO:2001242) is directly involved in cell death. Further, the positive regulation of endoplasmic reticulum unfolded protein response (GO:1900103) and ERAD pathway (GO:0036503) are events associated with ER stress response, which is also implicated in viral virulence and pathogenesis [35]. In addition, the involvement of neutrophil degranulation pathway (R-HAS-6798695) suggests the activation of the inflammatory

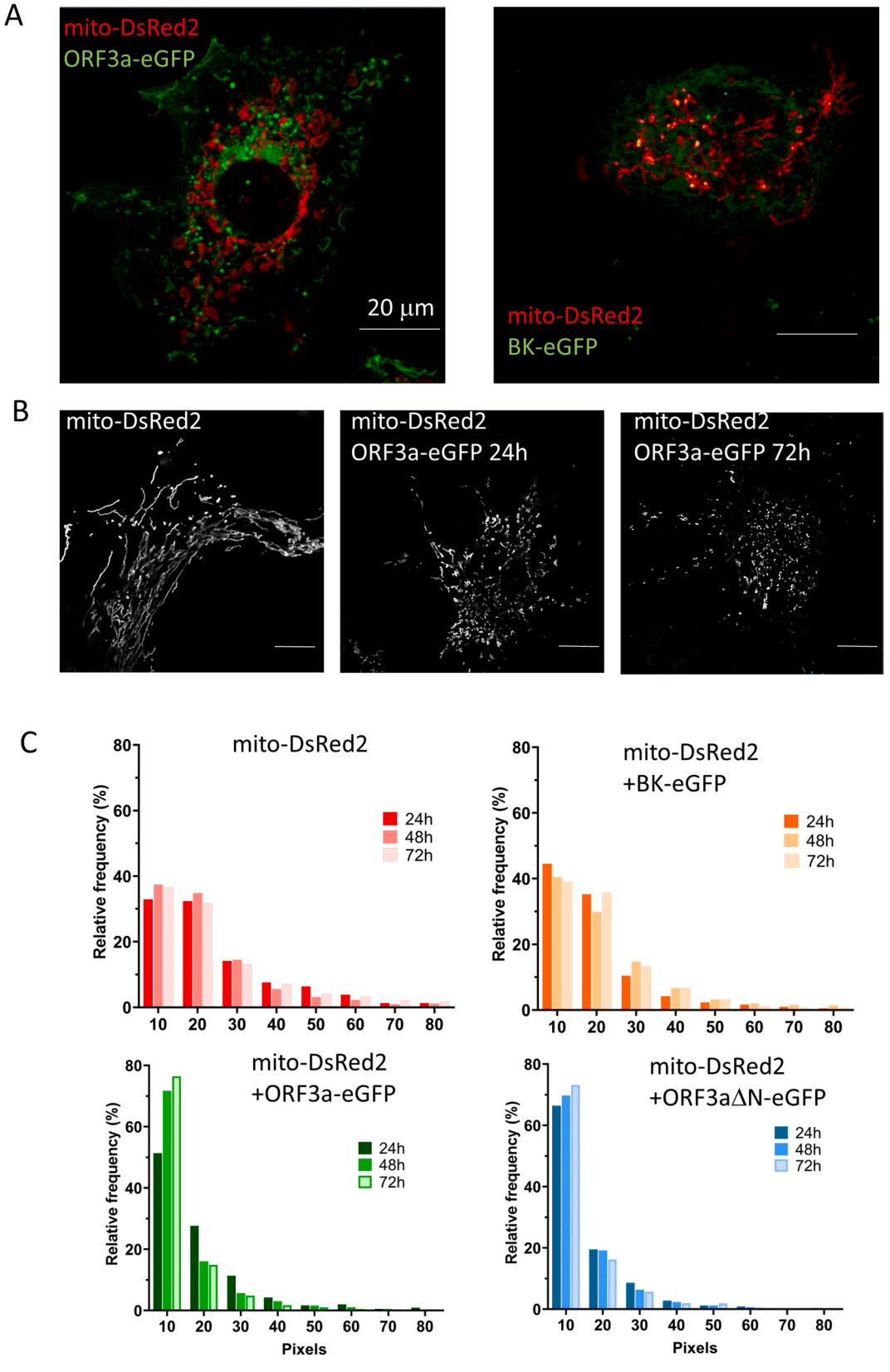

(caption on next page)

Fig. 7. Mitochondria fragmentation induced by ORF3a expression. (A) A representative COS7 cell transfected with ORF3a-eGFP and mito-DsRed2 (*left*) or BK-eGFP and mito-DsRed2 (*right*) showing how BK colocalizes with mitochondria marker while ORF3a does not colocalize. (B) Mitochondria morphology 24 h after transfection of mito-DsRed2 (*left*), co-transfection of ORF3a-eGFP and mito-DsRed2 (*middle*), or 72 h after co-transfection of ORF3a-eGFP and mito-DsRed2 (*right*). Scale bar = 20 μm. (C) Histograms representing the distribution of the mitochondria entities area (in pixels) at 24, 48 and 72 h after transfection of mito-DsRed2 (red), mito-DsRed2 and ORF3a-eGFP (green), mito-DsRed2 and ORF3aΔN-eGFP (blue), and mito-DsRed2 and BK-eGFP (orange).

response, a common occurrence during viral infection, including SARS-CoV-2 [36].

It is quite remarkable that 55 out of 192 proteins proximal to ORF3a and 4 out of 10 most enriched GO terms were associated with mitochondria (Fig. 6B, Table S1), suggesting that expression of ORF3a might influence mitochondria biology in infected cells. This unexpected result prompted us to explore the potential influence of ORF3a on mitochondria using live imaging approaches.

3.5. Mitochondrial fragmentation mediated by ORF3a variants

To study how mitochondria respond to ORF3a, we co-transfected the ORF3a-eGFP construct with mito-DsRed2, a marker of mitochondria that contains a DsRed2 fluorescent protein with a mitochondrial targeting sequence, known to preserve normal mitochondria physiology [37]. Fig. 7A shows the fluorescence detected in a cell transfected with mito-DsRed2 and ORF3a-eGFP, 24 h after transfection (left panel). The red and green fluorescence signals represent mitochondria and ORF3a, respectively. We did not detect colocalization between the ORF3a-eGFP with the mito-DsRed2, showing that the ORF3a protein does not traffic to the mitochondria. As a control of colocalization with the mito-DsRed2, we used the BK-eGFP ion channel (Fig. 7A, right panel). In this case, colocalization between the mito-DsRed2 and the BK channel was detected in many mitochondria.

Even though there was no colocalization of ORF3a with mitochondria, over time we did observe changes in the morphology of the mitochondria in cells expressing ORF3a. Fig. 7B compares the mito-DsRed2 fluorescence of cells expressing only the mitochondria marker 24 h after transfection (*left*), cells expressing the ORF3a-eGFP and the mito-DsRed2 marker 24 h after transfection (*middle*) and cells expressing the ORF3a-eGFP and the mito-DsRed2 marker 72 h after transfection (*right*). Clearly, ORF3a induces robust mitochondrial fragmentation, even after 24 h from the transfection. Mitochondria are dynamic structures that undergo fusion and fission cycles in response to the cell energy demands and the cellular environment [38,39]. Extensive mitochondrial fragmentation is also observed during apoptosis, preceding caspase activation [40,41]. To assess mitochondria fragmentation, we quantified the mitochondria area in cells transfected with the mito-DsRed2 marker with or without ORF3a. For the quantification, we used a custom Matlab/Octave software to isolate the mitochondria entities and measured their area as the number of pixels contained. For each condition, we collected images from multiple fields to collect more than 1500 mitochondria entities for analysis. Fig. 7C shows the histograms displaying the relative frequency of the number of pixels per entity collected 24, 48 or 72 h after transfection. In cells transfected only with mito-DsRed2, the distributions remained similar over time. This indicates that transfection of the marker did not induce mitochondria fragmentation. However, when the cells were transfected with the ORF3a-eGFP variant, we observed two noticeable differences. First, the overall distributions at the three time points are shifted towards the smaller areas, and second, over time the relative frequency of the smallest area increased from ~50% to ~75% over the three-day period, indicating progressive mitochondrial fragmentation. Similar results were observed when cells were transfected with the ORF3aΔN-eGFP variant (Fig. 7C). To rule out the possibility that overexpression of a membrane protein induces mitochondrial fragmentation, we used the BK channel construct as a control. In cells expressing BK-eGFP, the overall distributions of areas remained stable over the 72-h period (Fig. 7C). In addition, the relative frequencies of the smallest mitochondria entities were lower than those from ORF3a variants, and comparable to those from the cells transfected with mito-DsRed2 alone (Fig. 7C). These results demonstrate that overexpression of membrane proteins is not the cause of mitochondria fragmentation.

4. Discussion

SARS-CoV-2 ORF3a has been proposed to function as a viroporin, involved in the replication and release of the virus. It has also been related to apoptosis, necrosis and pyroptosis, contributing to tissue damage and thereby affecting the severity of COVID-19. A comprehension review of these functions and consequences has been recently published [42]. Here we study the stoichiometry, the ion channel activity, the trafficking and the interactome of SARS-CoV-2 ORF3a in human cells.

Our observations indicate that at the cell surface of HEK293 cells, SARS-CoV-2 ORF3a is most abundant as monomers and dimers. This differs from experiments done in insect cells, where the dimers and tetramers were the main types of complexes of ORF3a [4,5,43]. Because the ORF3aΔN-eGFP variant expressed more robustly at the cell surface, we found not only dimers and tetramers but also trimers and pentamers, which have not been reported previously. The dimeric structure [4] is remarkably stable by virtue of the ~140 methyl-methyl interactions between the two monomers [44]. Thereby, it is possible that the presence of monomers aroused by destabilization forces originated by the presence of the fluorescent protein tags used in this study. Irrespectively, these monomers are somehow stable in the lipid bilayer, which raises the question concerning the nature of the interactions between a dimeric interface and the lipids it is facing. For ORF3a, this is an interesting question because the so-called upper tunnel has a hydrophilic surface connecting the dimer interface with the lipid bilayer [4]. Yet, lacking a structure of a monomer form in a lipid environment, makes it difficult to have reasonable hypotheses.

The ORF3a protein was initially thought to be a viroporin based on electrophysiological experiments using *Xenopus* oocytes

overexpressing SARS-CoV ORF3a showing the presence of ionic currents [5] that were absent in control oocytes. However, using the homolog SARS-CoV-2 ORF3a, we were unable to reproduce those observations under similar experimental conditions. Further, we did not detect ionic currents in mammalian HEK293 cells expressing fluorescently tagged ORF3a protein at the cell surface that differ from the ionic currents detected in mock transfected cells, either in whole-cell and excised inside-out patch configurations. Similar observations were obtained in cells overexpressing ORF3aΔN protein, which was more efficiently targeted to the cell membrane. Furthermore, comparable results were reported by Miller et al. [43], a group with vast electrophysiological expertise. Miller and his colleagues also solved a series of cryo-EM structures of ORF3a dimers that unlikely represent membrane proteins permeable to K^+ or other cations. It has been suggested that the small ionic currents previously detected in *Xenopus* oocytes injected with ORF3a [5,8] could be attributed to endogenous calcium activated chloride channel [43,45,46]. Thereby, we propose, as [43] also do, that ORF3a at the cell surface is not an ion channel. Nonetheless, it is still possible that the protein functions as a viroporin within intracellular organelles and the ion channel activity detected in protoliposomes [4] might reflect those conditions. Interestingly, the SARS-CoV-2 ORF3a dimeric structure [4] is remarkably similar to the newly solved SARS-CoV-2 membrane protein M [47], as it was previously predicted [48,49]. Both proteins have similarities that suggest a common origin [50], with Protein M being conserved while ORF3a represents a variable form of the protein. Unlike ORF3a, protein M is not classified as a viroporin; instead, it is a structural protein that produce effects similar to those reported for ORF3a, such as apoptosis induction [51], alterations in the endomembranes, and mitochondrial fragmentation [19]. These results support the idea that viroporin activity is not necessary for ORF3a to increase of cell death in HEK293 cells. Here, we observed that 20–35% of HEK293 cells overexpressing the ORF3a-mCherry variant are prompt to dye after 48 h from transfection, substantially larger than the 3–7% of cell death observed in HEK293 cells overexpressing cytosolic mCherry alone. Presumably, none of the cells overexpressing ORF3a-mCherry exhibited viroporin activity at their cell surface.

SARS-CoV-2 ORF3a is expressed in several intracellular organelles of mammalian cells, including the ER, the Golgi, and the lysosomes. Our observations indicate that SARS-CoV-2 ORF3a follows a canonical membrane protein expression pathway. Its presence in the plasma membrane and endosomes is rare, except in the case of the ORF3aΔN variant. The high colocalization of the ORF3a protein with the lysosome marker is consistent with its involvement in lysosomal exocytosis for virus release [33] and autophagy inhibition [13,52].

Our work shows that combining a conditional proximity labeling method with the sensitive ascorbate peroxidase APEX2 enables a biotin tagging approach that effectively label proteins within the ORF3a vicinity. Many of the proteins identified by mass spectrometry are known to be related to functional observations associated with ORF3a. Our bioinformatic analysis unveiled that ORF3a may interact with various pathways and thereby participate into multiple biological processes within host cells. Consistent with our findings that ORF3a induced a robust increase in cell death (Fig. 4), several proteins associated with the regulation of intrinsic apoptotic signaling pathway (GO:2001242) were found to be proximal to ORF3a (Fig. 6C, Table S3). For instance, BAG5 (Bcl-2-Associated Athanogene 5), PPIA (Peptidyl-prolyl *cis*-trans isomerase A), PTPMT1 (Protein tyrosine phosphatase, mitochondrial 1), PTPN2 (Tyrosine-protein phosphatase non-receptor type 2) and ZNF385A (Zinc finger protein 385A) have been reported to suppress apoptotic process or prompt cell survival in various cells [53–57]. Even though the mechanistic interactions between these proximal proteins and ORF3a are unknown, their recruitment to the vicinity of ORF3a suggests a potential role for ORF3a as recruiter, akin to protein M. Hence, by recruiting these apoptosis suppressors, ORF3a might contribute to the weakening of host cells.

Viruses, including SARS-CoV-2, can hijack host lipid metabolic pathways to create an optimal environment for viral assembly and replication [58,59]. Consistent with this notion, our proximity assay identified three groups of biological processes related to lipid metabolism: Fatty acid metabolism (*R*-HSA:8978868), regulation of lipase activity (GO:0060191) and phospholipid biosynthetic process (GO:0008654) (Fig. 6C, Table S3).

An additional host cell metabolic process detected was the citric acid cycle, also known as the Krebs or tricarboxylic acid (TCA) cycle (GO:0006099), which is part of cellular respiration (GO:0045333) (Fig. 6C, Table S3). Not surprisingly, ATP synthesis is a major process targeted by viruses [60], including SARS-CoV-2 [61,62]. In the host cells, SARS-CoV-2 infection upregulates the expression of TCA cycle related proteins, such as isocitrate dehydrogenase 3 alpha IDH3A and gamma IDH3G [62], both of which were identified as proteins proximal to ORF3a based on our stringent criteria (Table S3). These results suggest that ORF3a may directly participate in regulating TCA cycle within the infected cells.

Another biological process detected was translation, including mitochondrial translation (*R*-HSA:5368287), mitochondrial translation elongation (*R*-HSA:5389840) and mitochondrial gene expression (GO:0140053), which are important for mitochondrial biogenesis (Fig. 6C, Table S3). These observations are in accordance with previous studies demonstrating that SARS-CoV-2 impairs mitochondrial biogenesis [63]. We identified 52 proximal mitochondria related proteins from the membrane fraction and 4 from the cytosolic fraction (Table S1). Interestingly, not even one is encoded by the mtDNA. These results suggest that ORF3a likely recruited these proteins while they were on their way to the mitochondria or after their release from the mitochondria. The fact that most of these proteins were pulled down from the membrane fraction indicates that they were effectively recruited either by ORF3a itself or other host proteins interacting with ORF3a. These results prompted us to study the status of mitochondria in cells overexpressing ORF3a. Clearly, ORF3a induced mitochondrial fission (Fig. 7), consistent with the detection of the PDZ domain-containing protein PDZD8 and the thioredoxin-related transmembrane protein TMX2 in the proximity of ORF3a (Table S1). Both PDZD8 and TMX2 are located at the mitochondria-ER contact sites (MERCS) [64,65]. PDZD8 functions as a critical tethering protein for the formation of MERCS sites [64], which are key regulators of the mitochondria fission↔fusion balance [66,67]. TMX2 deficiency leads to a reduction in mitochondrial spare respiratory capacity [65]. In addition to PDZD8 and TMX2, other MERCS related proteins were detected to be proximal to ORF3aΔN. Such as VAMP associated protein (VAPB), thioredoxin-related transmembrane protein (TMX1), long-chain acyl-coA synthetase (ACSL4) and BCR-associated protein (BCAP31) (Table S2). VAPB and TMX1 influence the number and size of MERCS [68,69], while ACSL4 plays a key role in MERCS sites during steroidogenesis [70]. BCAP31 is involved in the assembly of the

mitochondrial membrane respiratory chain, and the loss of BCAP31 results in mitochondrial fragmentation [71]. Even though these proteins were not identified as proximal proteins of ORF3a, they did show a tendency to be recruited by ORF3a, yet they did not meet the stringent p-value threshold (Table S1).

Using immunoprecipitation assays, ORF3a has been proposed to interact with the HOPS complex and consequently disrupt the fusion of autophagosomes with lysosomes [13,52]. Surprisingly, our data shows that none of the six components of HOPS complex (VPS41, VPS16, VPS39, VPS11, VPS33A, VPS18) was found in the proximity of ORF3a (Table S1). One difference between proximity labeling and traditional pulldown assays is that the former is performed in live cells while the latter is conducted with cell lysates. Additionally, the biotinylation reaction in proximity labeling is completed in 1 min whereas binding reactions in pulldown assays normally extend for half an hour or longer. These factors might have increased the chance of capturing the ORF3a-HOPS interactions using immunoprecipitation approaches. Another potential factor that may have affected our capability to detect any proximal protein from the HOPS complex is the presence of hydrogen peroxide, particularly when it disrupts protein-protein interactions. Indeed, it has been reported that H_2O_2 treatment impaired the fusion between autophagosomes and lysosomes [72], albeit their experimental conditions are drastically different from ours. Giving all the information discussed above, it is reasonable to hypothesize that the binding between ORF3a and the HOPS complex involves relatively weak interactions, which cannot be identified by the APEX2 proximity ligation method.

The APEX based proximity labeling approach used in our study offers several advantages. First, it enables high-throughput screening of viral-host interactions using live cells, minimizing the likelihood of false-positive detections resulting from artificial interactions that may occur due to cellular disruption. Second, the conditional proximity labeling method provides precise spatiotemporal control over labeling, thereby avoiding potential contamination arising from proteomic differences between ORF3a-expressing cells and controls. Third, it offers a snapshot of protein-protein interactions at a specific time point. However, the temporal specificity of the method means that interactions occurring at distinct time points may not be captured. Additionally, the use of hydrogen peroxide, even with a short incubation time of 1 min, may have its own effect on biological processes. These factors could affect the ability of the method to detect certain proteins reported to interact with ORF3a, such as the HOPS complex [15,43,73]. Moreover, it is worth noting that when the bait is a membrane protein and the APEX2 domain is cytosolic, like in our case, the method is limited to assessing interacting integral membrane proteins that share the location of the bait or interacting cytosolic proteins. Thereby proteins that interact with ORF3a in the lumen of the intracellular organelles in which it was present or proteins from the extracellular environment would fail to be detected. This limitation is because the reactant produced by APEX2 is impermeable to lipid bilayers. Thorough discussions of the scope of proximity labeling methods can be found elsewhere [74,75].

It is important to acknowledge that most of the ORF3a proteins detected in our study were in intracellular organelles, inaccessible to our electrophysiology experiments. Therefore, not detecting ionic currents mediated by ORF3a do not exclude the possibility that ORF3a exhibits viroporin-like activity in intracellular organelles but loses it before reaching the plasma membrane, possibly due to alterations in protein conformation or function. This could potentially explain the detection of ionic currents mediated by ORF3a in reconstituted proteoliposomes [4], albeit similar approaches with similar results showed that these single channel currents are likely originated by leak and/or channel contamination [43].

In summary, we have described the stoichiometry and expression pattern of the SARS-Cov-2 ORF3a in mammalian cells, showing an increase in cell death through apoptosis activation accompanied by mitochondrial fragmentation. We found no indication of ion channel activity by any of the tested ORF3a constructs in the cell membrane. Finally, we have elucidated the proteomic vicinity of ORF3a uncovering multiple pathways relevant to viral infection and mitochondrial dynamics. These results combined suggest that ORF3a exerts a broad influence on the biology of the host mammalian cells.

Author contribution statement

Song Jiao, Pablo Miranda: Conceived and designed the experiments; Performed the experiments; Analyzed and interpreted the data; Wrote the paper.

Yan Li, Dragan Maric: Performed the experiments; Analyzed and interpreted the data; Wrote the paper.

Miguel Holmgren: Conceived and designed the experiments; Wrote the paper.

Funding statement

Song Jiao, Pablo Miranda, Yan Li, Dragan Maric, and Miguel Holmgren were supported by the Intramural Research Program of the NIH (National Institute of Neurological Disorders and Stroke).

Data availability statement

- The Mass spectrometry data and search results have been deposited at the ProteomeXchange Consortium with the dataset identifiers (ProteomeXchange: PXD039372 and PXD039373) and are publicly available as of the date of publication. All data reported in this paper will be shared by the lead contact upon request.
- The original code for mitochondrial fragments analysis has been deposited at the Mendeley Data with the DOI: 10.17632/xbfc3ngbk4.1 and is publicly available as of the date of publication.
- Any additional information required to reanalyze the data reported in this paper is available from the lead contact upon request.

Declaration of competing interest

The authors declare that they have no known competing financial interests or personal relationships that could have appeared to influence the work reported in this paper.

Appendix A. Supplementary data

Supplementary data to this article can be found online at https://doi.org/10.1016/j.heliyon.2023.e18754.

References

[1] P. Zhou, X.L. Yang, X.G. Wang, B. Hu, L. Zhang, W. Zhang, H.R. Si, Y. Zhu, B. Li, C.L. Huang, H.D. Chen, J. Chen, Y. Luo, H. Guo, R.D. Jiang, M.Q. Liu, Y. Chen, X.R. Shen, X. Wang, X.S. Zheng, K. Zhao, Q.J. Chen, F. Deng, L.L. Liu, B. Yan, F.X. Zhan, Y.Y. Wang, G.F. Xiao, Z.L. Shi, A pneumonia outbreak associated with a new coronavirus of probable bat origin, Nature 579 (2020) 270–273, https://doi.org/10.1038/s41586-020-2012-7.

[2] A. Rahimi, A. Mirzazadeh, S. Tavakolpour, Genetics and genomics of SARS-CoV-2: a review of the literature with the special focus on genetic diversity and SARS-CoV-2 genome detection, Genomics 113 (2021) 1221–1232, https://doi.org/10.1016/j.ygeno.2020.09.059.

[3] E. Issa, G. Merhi, B. Panossian, T. Salloum, S. Tokajian, SARS-CoV-2 and ORF3a: nonsynonymous mutations, functional domains, and viral pathogenesis, mSystems 5 (2020), https://doi.org/10.1128/mSystems.00266-20.

[4] D.M. Kern, B. Sorum, S.S. Mali, C.M. Hoel, S. Sridharan, J.P. Remis, D.B. Toso, A. Kotecha, D.M. Bautista, S.G. Brohawn, Cryo-EM structure of SARS-CoV-2 ORF3a in lipid nanodiscs, Nat. Struct. Mol. Biol. 28 (2021) 573–582, https://doi.org/10.1038/s41594-021-00619-0.

[5] W. Lu, B.J. Zheng, K. Xu, W. Schwarz, L. Du, C.K. Wong, J. Chen, S. Duan, V. Deubel, B. Sun, Severe acute respiratory syndrome-associated coronavirus 3a protein forms an ion channel and modulates virus release, Proc. Natl. Acad. Sci. U. S. A. 103 (2006) 12540–12545, https://doi.org/10.1073/pnas.0605402103.

[6] M. Ramjeesingh, L.J. Huan, E. Garami, C.E. Bear, Novel method for evaluation of the oligomeric structure of membrane proteins, Biochem. J. 342 (1) (1999) 119–123.

[7] C.M. Chan, H. Tsoi, W.M. Chan, S. Zhai, C.O. Wong, X. Yao, W.Y. Chan, S.K. Tsui, H.Y. Chan, The ion channel activity of the SARS-coronavirus 3a protein is linked to its pro-apoptotic function, Int. J. Biochem. Cell Biol. 41 (2009) 2232–2239, https://doi.org/10.1016/j.biocel.2009.04.019.

[8] T.L. Toft-Bertelsen, M.G. Jeppesen, E. Tzortzini, K. Xue, K. Giller, S. Becker, A. Mujezinovic, B.H. Bentzen, B.A. L, A. Kolocouris, T.N. Kledal, M.M. Rosenkilde, Amantadine has potential for the treatment of COVID-19 because it inhibits known and novel ion channels encoded by SARS-CoV-2, Commun. Biol. 4 (2021) 1347, https://doi.org/10.1038/s42003-021-02866-9.

[9] S. Gargan, N.J. Stevenson, Unravelling the immunomodulatory effects of viral ion channels, towards the treatment of disease, Viruses 13 (2021), https://doi.org/10.3390/v13112165.

[10] X. Zhang, Z. Yang, T. Pan, X. Long, Q. Sun, P.H. Wang, X. Li, E. Kuang, SARS-CoV-2 ORF3a induces RETREG1/FAM134B-dependent reticulophagy and triggers sequential ER stress and inflammatory responses during SARS-CoV-2 infection, Autophagy (2022) 1–17, https://doi.org/10.1080/15548627.2022.2039992.

[11] R. Minakshi, K. Padhan, The YXXPhi motif within the severe acute respiratory syndrome coronavirus (SARS-CoV) 3a protein is crucial for its intracellular transport, Virol. J. 11 (2014) 75, https://doi.org/10.1186/1743-422X-11-75.

[12] Y.J. Tan, E. Teng, S. Shen, T.H. Tan, P.Y. Goh, B.C. Fielding, E.E. Ooi, H.C. Tan, S.G. Lim, W. Hong, A novel severe acute respiratory syndrome coronavirus protein, U274, is transported to the cell surface and undergoes endocytosis, J. Virol. 78 (2004) 6723–6734, https://doi.org/10.1128/JVI.78.13.6723-6734.2004.

[13] Y. Zhang, H. Sun, R. Pei, B. Mao, Z. Zhao, H. Li, Y. Lin, K. Lu, The SARS-CoV-2 protein ORF3a inhibits fusion of autophagosomes with lysosomes, Cell. Discov. 7 (2021) 31, https://doi.org/10.1038/s41421-021-00268-z.

[14] S. Ghosh, T.A. Dellibovi-Ragheb, A. Kerviel, E. Pak, Q. Qiu, M. Fisher, P.M. Takvorian, C. Bleck, V.W. Hsu, A.R. Fehr, S. Perlman, S.R. Achar, M.R. Straus, G. R. Whittaker, C.A.M. de Haan, J. Kehrl, G. Altan-Bonnet, N. Altan-Bonnet, Beta-coronaviruses use lysosomes for egress instead of the biosynthetic secretory pathway, Cell 183 (2020) 1520–1535, https://doi.org/10.1016/j.cell.2020.10.039.

[15] D.E. Gordon, G.M. Jang, M. Bouhaddou, J. Xu, K. Obernier, K.M. White, M.J. O'Meara, V.V. Rezelj, J.Z. Guo, D.L. Swaney, T.A. Tummino, R. Huttenhain, R. M. Kaake, A.L. Richards, B. Tutuncuoglu, H. Foussard, J. Batra, K. Haas, M. Modak, M. Kim, P. Haas, B.J. Polacco, H. Braberg, J.M. Fabius, M. Eckhardt, M. Soucheray, M.J. Bennett, M. Cakir, M.J. McGregor, Q. Li, B. Meyer, F. Roesch, T. Vallet, A. Mac Kain, L. Miorin, E. Moreno, Z.Z.C. Naing, Y. Zhou, S. Peng, Y. Shi, Z. Zhang, W. Shen, I.T. Kirby, J.E. Melnyk, J.S. Chorba, K. Lou, S.A. Dai, I. Barrio-Hernandez, D. Memon, C. Hernandez-Armenta, J. Lyu, C.J.P. Mathy, T. Perica, K.B. Pilla, S.J. Ganesan, D.J. Saltzberg, R. Rakesh, X. Liu, S.B. Rosenthal, L. Calviello, S. Venkataramanan, J. Liboy-Lugo, Y. Lin, X.P. Huang, Y. Liu, S. A. Wankowicz, M. Bohn, M. Safari, F.S. Ugur, C. Koh, N.S. Savar, Q.D. Tran, D. Shengjuler, S.J. Fletcher, M.C. O'Neal, Y. Cai, J.C.J. Chang, D.J. Broadhurst, S. Klippsten, P.P. Sharp, N.A. Wenzell, D. Kuzuoglu-Ozturk, H.Y. Wang, R. Trenker, J.M. Young, D.A. Cavero, J. Hiatt, T.L. Roth, U. Rathore, A. Subramanian, J. Noack, M. Hubert, R.M. Stroud, A.D. Frankel, O.S. Rosenberg, K.A. Verba, D.A. Agard, M. Ott, M. Emerman, N. Jura, M. von Zastrow, E. Verdin, A. Ashworth, O. Schwartz, C. d'Enfert, S. Mukherjee, M. Jacobson, H.S. Malik, D.G. Fujimori, T. Ideker, C.S. Craik, S.N. Floor, J.S. Fraser, J.D. Gross, A. Sali, B.L. Roth, D. Ruggero, J. Taunton, T. Kortemme, P. Beltrao, M. Vignuzzi, A. Garcia-Sastre, K.M. Shokat, B.K. Shoichet, N.J. Krogan, A SARS-CoV-2 protein interaction map reveals targets for drug repurposing, Nature 583 (2020) 459–468, https://doi.org/10.1038/s41586-020-2286-9.

[16] J. Li, M. Guo, X. Tian, X. Wang, X. Yang, P. Wu, C. Liu, Z. Xiao, Y. Qu, Y. Yin, C. Wang, Y. Zhang, Z. Zhu, Z. Liu, C. Peng, T. Zhu, Q. Liang, Virus-host interactome and proteomic survey reveal potential virulence factors influencing SARS-CoV-2 pathogenesis, Méd. 2 (2021) 99–112 e117, https://doi.org/10.1016/j.medj.2020.07.002.

[17] V. Hung, N.D. Udeshi, S.S. Lam, K.H. Loh, K.J. Cox, K. Pedram, S.A. Carr, A.Y. Ting, Spatially resolved proteomic mapping in living cells with the engineered peroxidase APEX2, Nat. Protoc. 11 (2016) 456–475, https://doi.org/10.1038/nprot.2016.018.

[18] J.R. St-Germain, A. Astori, P. Samavarchi-Tehrani, H. Abdouni, V. Macwan, D.-K. Kim, J.J. Knapp, F.P. Roth, A.-C. Gingras, B. Raught, A SARS-CoV-2 BioID-Based Virus-Host Membrane Protein Interactome and Virus Peptide Compendium: New Proteomics Resources for COVID-19 Research, 2020, https://doi.org/10.1101/2020.08.28.269175.

[19] Y.-B. Lee, M. Jung, J. Kim, M.-G. Kang, C. Kwak, J.-S. Kim, J.-Y. Mun, H.-W. Rhee, Endomembrane systems are reorganized by ORF3a and Membrane, (M) of SARS-CoV-2 (2021), https://doi.org/10.1101/2021.06.01.446555.

[20] P. Samavarchi-Tehrani, H. Abdouni, J.D.R. Knight, A. Astori, R. Samson, Z.-Y. Lin, D.-K. Kim, J.J. Knapp, J. St-Germain, C.D. Go, B. Larsen, C.J. Wong, P. Cassonnet, C. Demeret, Y. Jacob, F.P. Roth, B. Raught, A.-C. Gingras, A SARS-CoV-2, host proximity interactome (2020), https://doi.org/10.1101/2020.09.03.282103.

[21] J. Birnbaum, S. Scharf, S. Schmidt, E. Jonscher, W.A.M. Hoeijmakers, S. Flemming, C.G. Toenhake, M. Schmitt, R. Sabitzki, B. Bergmann, U. Frohlke, P. Mesen-Ramirez, A. Blancke Soares, H. Herrmann, R. Bartfai, T. Spielmann, A Kelch13-defined endocytosis pathway mediates artemisinin resistance in malaria parasites, Science 367 (2020) 51–59, https://doi.org/10.1126/science.aax4735.

[22] S.R. Wilmington, A. Matouschek, An inducible system for rapid degradation of specific cellular proteins using proteasome adaptors, PLoS One 11 (2016), e0152679, https://doi.org/10.1371/journal.pone.0152679.

[23] M. Muller, C. James, C. Lenz, H. Urlaub, R.H. Kehlenbach, Probing the environment of emerin by enhanced ascorbate peroxidase 2 (APEX2)-Mediated proximity labeling, Cells 9 (2020), https://doi.org/10.3390/cells9030605.

[24] M.M. Chertkova Ao, M. Postma, N. van Bommel, S. van der Niet, K.L. Batenburg, L. Joosen, T.W.J. Gadella, Y. Okada, J. Goedhart, Robust and bright genetically encoded fluorescent markers for highlighting structures and compartments in mammalian cells, bioRxiv (2017), https://doi.org/10.1101/160374.

[25] X. Liu, F. Fagotto, A method to separate nuclear, cytosolic, and membrane-associated signaling molecules in cultured cells, Sci. Signal. 4 (2011).

[26] S.X. Ge, D. Jung, R. Yao, ShinyGO: a graphical gene-set enrichment tool for animals and plants, Bioinformatics 36 (2020) 2628–2629, https://doi.org/10.1093/bioinformatics/btz931.

[27] H. Mi, D. Ebert, A. Muruganujan, C. Mills, L.P. Albou, T. Mushayamaha, P.D. Thomas, PANTHER version 16: a revised family classification, tree-based classification tool, enhancer regions and extensive API, Nucleic Acids Res 49 (2021) D394–D403, https://doi.org/10.1093/nar/gkaa1106.

[28] G. Bindea, B. Mlecnik, H. Hackl, P. Charoentong, M. Tosolini, A. Kirilovsky, W.H. Fridman, F. Pages, Z. Trajanoski, J. Galon, ClueGO: a Cytoscape plug-in to decipher functionally grouped gene ontology and pathway annotation networks, Bioinformatics 25 (2009) 1091–1093, https://doi.org/10.1093/bioinformatics/btp101.

[29] G. Bindea, J. Galon, B. Mlecnik, CluePedia Cytoscape plugin: pathway insights using integrated experimental and in silico data, Bioinformatics 29 (2013) 661–663, https://doi.org/10.1093/bioinformatics/btt019.

[30] P. Shannon, A. Markiel, O. Ozier, N.S. Baliga, J.T. Wang, D. Ramage, N. Amin, B. Schwikowski, T. Ideker, Cytoscape: a software environment for integrated models of biomolecular interaction networks, Genome Res. 13 (2003) 2498–2504, https://doi.org/10.1101/gr.1239303.

[31] R. Wiese, M. Eiglsperger, M. Kaufmann, Yfiles: visualization and automatic layout of graphs, Lect. Notes Comput. Sci. 2265 (2002) 453–454.

[32] L. Santacruz-Toloza, Y. Huang, S.A. John, D.M. Papazian, Glycosylation of Shaker potassium channel protein in insect cell culture and in Xenopus oocytes, Biochemistry 33 (1994) 5607–5613, https://doi.org/10.1021/bi00184a033,.

[33] D. Chen, Q. Zheng, L. Sun, M. Ji, Y. Li, H. Deng, H. Zhang, ORF3a of SARS-CoV-2 promotes lysosomal exocytosis-mediated viral egress, Dev. Cell 56 (2021) 3250–3263, https://doi.org/10.1016/j.devcel.2021.10.006.

[34] C.D. Bortner, J.A. Cidlowski, Apoptotic volume decrease and the incredible shrinking cell, Cell Death Differ. 9 (2002) 1307–1310, https://doi.org/10.1038/sj.cdd.4401126.

[35] S. Li, L. Kong, X. Yu, The expanding roles of endoplasmic reticulum stress in virus replication and pathogenesis, Crit. Rev. Microbiol. 41 (2015) 150–164, https://doi.org/10.3109/1040841X.2013.813899.

[36] L.F. Garcia, Immune response, inflammation, and the clinical spectrum of COVID-19, Front. Immunol. 11 (2020) 1441, https://doi.org/10.3389/fimmu.2020.01441.

[37] N. Ohno, G.J. Kidd, D. Mahad, S. Kiryu-Seo, A. Avishai, H. Komuro, B.D. Trapp, Myelination and axonal electrical activity modulate the distribution and motility of mitochondria at CNS nodes of Ranvier, J. Neurosci. 31 (2011) 7249–7258, https://doi.org/10.1523/JNEUROSCI.0095-11.2011.

[38] R.J. Youle, A.M. van der Bliek, Mitochondrial fission, fusion, and stress, Science 337 (2012) 1062–1065, https://doi.org/10.1126/science.1219855.

[39] M. Adebayo, S. Singh, A.P. Singh, S. Dasgupta, Mitochondrial fusion and fission: the fine-tune balance for cellular homeostasis, Faseb. J. 35 (2021), e21620, https://doi.org/10.1096/fj.202100067R.

[40] D.F. Suen, K.L. Norris, R.J. Youle, Mitochondrial dynamics and apoptosis, Genes Dev. 22 (2008) 1577–1590, https://doi.org/10.1101/gad.1658508.

[41] Y.J. Lee, S.Y. Jeong, M. Karbowski, C.L. Smith, R.J. Youle, Roles of the mammalian mitochondrial fission and fusion mediators Fis1, Drp 1, and Opa1 in apoptosis, Mol. Biol. Cell 15 (2004) 5001–5011, https://doi.org/10.1091/mbc.e04-04-0294.

[42] J. Zhang, A. Ejikemeuwa, V. Gerzanich, M. Nasr, Q. Tang, J.M. Simard, R.Y. Zhao, Understanding the role of SARS-CoV-2 ORF3a in viral pathogenesis and COVID-19, Front. Microbiol. 13 (2022), 854567, https://doi.org/10.3389/fmicb.2022.854567.

[43] A.N. Miller, P.R. Houlihan, E. Matamala, D. Cabezas-Bratesco, G.Y. Lee, B. Cristofori-Armstrong, T.L. Dilan, S. Sanchez-Martinez, D. Matthies, R. Yan, Z. Yu, D. Ren, S.E. Brauchi, D.E. Clapham, The SARS-CoV-2 accessory protein ORF3a is not an ion channel, but does interact with trafficking proteins, Elife 12 (2023), e84477, https://doi.org/10.7554/eLife.84477.

[44] V. Marquez-Miranda, M. Rojas, Y. Duarte, I. Diaz-Franulic, M. Holmgren, R.E. Cachau, F.D. Gonzalez-Nilo, Analysis of SARS-CoV-2 ORF3a structure reveals chloride binding sites, bioRxiv (2020), https://doi.org/10.1101/2020.10.22.349522.

[45] N.L. Harrison, G.W. Abbott, M. Gentzsch, A. Aleksandrov, A. Moroni, G. Thiel, S. Grant, C.G. Nichols, H.A. Lester, A. Hartel, K. Shepard, D.C. Garcia, M. Yazawa, How many SARS-CoV-2 "viroporins" are really ion channels? Commun. Biol. 5 (2022) 859, https://doi.org/10.1038/s42003-022-03669-2.

[46] T.L. Toft-Bertelsen, M.G. Jeppesen, A. Landbrug, A. Mujezinovic, B.H. Bentzen, T.N. Kledal, M.M. Rosenkilde, Reply to: how many SARS-CoV-2 "viroporins" are really ion channels? Commun. Biol. 5 (2022) 860, https://doi.org/10.1038/s42003-022-03670-9.

[47] Z. Zhang, N. Nomura, Y. Muramoto, T. Ekimoto, T. Uemura, K. Liu, M. Yui, N. Kono, J. Aoki, M. Ikeguchi, T. Noda, S. Iwata, U. Ohto, T. Shimizu, Structure of SARS-CoV-2 membrane protein essential for virus assembly, Nat. Commun. 13 (2022) 4399, https://doi.org/10.1038/s41467-022-32019-3.

[48] S. Thomas, The structure of the membrane protein of SARS-CoV-2 resembles the sugar transporter SemiSWEET, Pathog. Immun. 5 (2020) 342–363, https://doi.org/10.20411/pai.v5i1.377.

[49] C. Marques-Pereira, M.N. Pires, R.P. Gouveia, N.N. Pereira, A.B. Caniceiro, N. Rosario-Ferreira, I.S. Moreira, SARS-CoV-2 membrane protein: from genomic data to structural new insights, Int. J. Mol. Sci. 23 (2022), https://doi.org/10.3390/ijms23062986.

[50] C.A. Ouzounis, A recent origin of Orf3a from M protein across the coronavirus lineage arising by sharp divergence, Comput. Struct. Biotechnol. J. 18 (2020) 4093–4102, https://doi.org/10.1016/j.csbj.2020.11.047.

[51] P. Kumar, A. Kumar, N. Garg, R. Giri, An insight into SARS-CoV-2 membrane protein interaction with spike, envelope, and nucleocapsid proteins, J. Biomol. Struct. Dyn. (2021) 1–10, https://doi.org/10.1080/07391102.2021.2016490.

[52] G. Miao, H. Zhao, Y. Li, M. Ji, Y. Chen, Y. Shi, Y. Bi, P. Wang, H. Zhang, ORF3a of the COVID-19 virus SARS-CoV-2 blocks HOPS complex-mediated assembly of the SNARE complex required for autolysosome formation, Dev. Cell 56 (2021) 427–442 e425, https://doi.org/10.1016/j.devcel.2020.12.010.

[53] A. Bruchmann, C. Roller, T.V. Walther, G. Schafer, S. Lehmusvaara, T. Visakorpi, H. Klocker, A.C. Cato, D. Maddalo, Bcl-2 associated athanogene 5 (Bag5) is overexpressed in prostate cancer and inhibits ER-stress induced apoptosis, BMC Cancer 13 (2013) 96, https://doi.org/10.1186/1471-2407-13-96.

[54] S. Cheng, M. Luo, C. Ding, C. Peng, Z. Lv, R. Tong, H. Xiao, H. Xie, L. Zhou, J. Wu, S. Zheng, Downregulation of Peptidylprolyl isomerase A promotes cell death and enhances doxorubicin-induced apoptosis in hepatocellular carcinoma, Gene 591 (2016) 236–244, https://doi.org/10.1016/j.gene.2016.07.020.

[55] N.M. Niemi, N.J. Lanning, L.M. Westrate, J.P. MacKeigan, Downregulation of the mitochondrial phosphatase PTPMT1 is sufficient to promote cancer cell death, PLoS One 8 (2013), e53803, https://doi.org/10.1371/journal.pone.0053803.

[56] I. Santin, F. Moore, M.L. Colli, E.N. Gurzov, L. Marselli, P. Marchetti, D.L. Eizirik, PTPN2, a candidate gene for type 1 diabetes, modulates pancreatic beta-cell apoptosis via regulation of the BH3-only protein Bim, Diabetes 60 (2011) 3279–3288, https://doi.org/10.2337/db11-0758.

[57] S. Das, L. Raj, B. Zhao, Y. Kimura, A. Bernstein, S.A. Aaronson, S.W. Lee, Hzf Determines cell survival upon genotoxic stress by modulating p53 transactivation, Cell 130 (2007) 624–637, https://doi.org/10.1016/j.cell.2007.06.013.

[58] I. Perez-Torres, V. Guarner-Lans, E. Soria-Castro, L. Manzano-Pech, A. Palacios-Chavarria, R.R. Valdez-Vazquez, J.G. Dominguez-Cherit, H. Herrera-Bello, H. Castillejos-Suastegui, L. Moreno-Castaneda, G. Alanis-Estrada, F. Hernandez, O. Gonzalez-Marcos, R. Marquez-Velasco, M.E. Soto, Alteration in the lipid profile and the desaturases activity in patients with severe pneumonia by SARS-CoV-2, Front. Physiol. 12 (2021), 667024, https://doi.org/10.3389/fphys.2021.667024.

[59] N.S. Heaton, G. Randall, Multifaceted roles for lipids in viral infection, Trends Microbiol. 19 (2011) 368–375, https://doi.org/10.1016/j.tim.2011.03.007.

[60] F.J. Sanchez-Garcia, C.A. Perez-Hernandez, M. Rodriguez-Murillo, M.M.B. Moreno-Altamirano, The role of tricarboxylic acid cycle metabolites in viral infections, Front. Cell. Infect. Microbiol. 11 (2021), 725043, https://doi.org/10.3389/fcimb.2021.725043.

[61] P.J. Mullen, G. Garcia Jr., A. Purkayastha, N. Matulionis, E.W. Schmid, M. Momcilovic, C. Sen, J. Langerman, A. Ramaiah, D.B. Shackelford, R. Damoiseaux, S. W. French, K. Plath, B.N. Gomperts, V. Arumugaswami, H.R. Christofk, SARS-CoV-2 infection rewires host cell metabolism and is potentially susceptible to mTORC1 inhibition, Nat. Commun. 12 (2021) 1876, https://doi.org/10.1038/s41467-021-22166-4.

[62] D. Bojkova, K. Klann, B. Koch, M. Widera, D. Krause, S. Ciesek, J. Cinatl, C. Munch, Proteomics of SARS-CoV-2-infected host cells reveals therapy targets, Nature 583 (2020) 469–472, https://doi.org/10.1038/s41586-020-2332-7.
[63] J.W. Guarnieri, J.M. Dybas, H. Fazelinia, M.S. Kim, J. Frere, Y. Zhang, Y.S. Albrecht, D.G. Murdock, A. Angelin, L.N. Singh, S.L. Weiss, S.M. Best, M.T. Lott, H. Cope, V. Zaksas, A. Saravia-Butler, C. Meydan, J. Foox, C. Mozsary, Y.H. Kidane, W. Priebe, M.R. Emmett, R. Meller, U. Singh, Y. Bram, B.R. tenOever, M. T. Heise, N.J. Moorman, E.A. Madden, S.A. Taft-Benz, E.J. Anderson, W.A. Sanders, R.J. Dickmander, V.K. Baxter, S.B. Baylin, E.S. Wurtele, P.M. Moraes-Vieira, D. Taylor, C.E. Mason, J.C. Schisler, R.E. Schwartz, A. Beheshti, D.C. Wallace, Targeted down regulation of Core mitochondrial genes during SARS-CoV-2 infection, bioRxiv (2022), https://doi.org/10.1101/2022.02.19.481089.
[64] Y. Hirabayashi, S.K. Kwon, H. Paek, W.M. Pernice, M.A. Paul, J. Lee, P. Erfani, A. Raczkowski, D.S. Petrey, L.A. Pon, F. Polleux, ER-mitochondria tethering by PDZD8 regulates Ca(2+) dynamics in mammalian neurons, Science 358 (2017) 623–630, https://doi.org/10.1126/science.aan6009.
[65] L.V. Vandervore, R. Schot, C. Milanese, D.J. Smits, E. Kasteleijn, A.E. Fry, D.T. Pilz, S. Brock, E. Borklu-Yucel, M. Post, N. Bahi-Buisson, M.J. Sanchez-Soler, M. van Slegtenhorst, B. Keren, A. Afenjar, S.A. Coury, W.H. Tan, R. Oegema, L.S. de Vries, K.A. Fawcett, P.G.J. Nikkels, A. Bertoli-Avella, A. Al Hashem, A. A. Alwabel, K. Tlili-Graiess, S. Efthymiou, F. Zafar, N. Rana, F. Bibi, H. Houlden, R. Maroofian, R.E. Person, A. Crunk, J.M. Savatt, L. Turner, M. Doosti, E. G. Karimiani, N.W. Saadi, J. Akhondian, M.H. Lequin, H. Kayserili, P.J. van der Spek, A.C. Jansen, J.M. Kros, R.M. Verdijk, N.J. Milosevic, M. Fornerod, P. G. Mastroberardino, G.M.S. Mancini, TMX2 is a crucial regulator of cellular redox state, and its dysfunction causes severe brain developmental abnormalities, Am. J. Hum. Genet. 105 (2019) 1126–1147, https://doi.org/10.1016/j.ajhg.2019.10.009.
[66] S. Aoyama-Ishiwatari, Y. Hirabayashi, Endoplasmic reticulum-mitochondria contact sites-emerging intracellular signaling hubs, Front. Cell Dev. Biol. 9 (2021), 653828, https://doi.org/10.3389/fcell.2021.653828.
[67] J.R. Friedman, L.L. Lackner, M. West, J.R. DiBenedetto, J. Nunnari, G.K. Voeltz, ER tubules mark sites of mitochondrial division, Science 334 (2011) 358–362, https://doi.org/10.1126/science.1207385.
[68] R. Stoica, K.J. De Vos, S. Paillusson, S. Mueller, R.M. Sancho, K.F. Lau, G. Vizcay-Barrena, W.L. Lin, Y.F. Xu, J. Lewis, D.W. Dickson, L. Petrucelli, J.C. Mitchell, C.E. Shaw, C.C. Miller, ER-mitochondria associations are regulated by the VAPB-PTPIP51 interaction and are disrupted by ALS/FTD-associated TDP-43, Nat. Commun. 5 (2014) 3996, https://doi.org/10.1038/ncomms4996.
[69] A. Raturi, T. Gutierrez, C. Ortiz-Sandoval, A. Ruangkittisakul, M.S. Herrera-Cruz, J.P. Rockley, K. Gesson, D. Ourdev, P.H. Lou, E. Lucchinetti, N. Tahbaz, M. Zaugg, S. Baksh, K. Ballanyi, T. Simmen, TMX1 determines cancer cell metabolism as a thiol-based modulator of ER-mitochondria Ca2+ flux, J. Cell Biol. 214 (2016) 433–444, https://doi.org/10.1083/jcb.201512077.
[70] A. Duarte, C. Poderoso, M. Cooke, G. Soria, F. Cornejo Maciel, V. Gottifredi, E.J. Podesta, Mitochondrial fusion is essential for steroid biosynthesis, PLoS One 7 (2012), e45829, https://doi.org/10.1371/journal.pone.0045829.
[71] T. Namba, BAP31 regulates mitochondrial function via interaction with Tom 40 within ER-mitochondria contact sites, Sci. Adv. 5 (2019), eaaw1386, https://doi.org/10.1126/sciadv.aaw1386.
[72] P. Jiang, Z. Huang, H. Zhao, T. Wei, Hydrogen peroxide impairs autophagic flux in a cell model of nonalcoholic fatty liver disease, Biochem. Biophys. Res. Commun. 433 (2013) 408–414, https://doi.org/10.1016/j.bbrc.2013.02.118.
[73] D.E. Gordon, J. Hiatt, M. Bouhaddou, V.V. Rezelj, S. Ulferts, H. Braberg, A.S. Jureka, K. Obernier, J.Z. Guo, J. Batra, R.M. Kaake, A.R. Weckstein, T.W. Owens, M. Gupta, S. Pourmal, E.W. Titus, M. Cakir, M. Soucheray, M. McGregor, Z. Cakir, G. Jang, M.J. O'Meara, T.A. Tummino, Z. Zhang, H. Foussard, A. Rojc, Y. Zhou, D. Kuchenov, R. Huttenhain, J. Xu, M. Eckhardt, D.L. Swaney, J.M. Fabius, M. Ummadi, B. Tutuncuoglu, U. Rathore, M. Modak, P. Haas, K.M. Haas, Z. Z.C. Naing, E.H. Pulido, Y. Shi, I. Barrio-Hernandez, D. Memon, E. Petsalaki, A. Dunham, M.C. Marrero, D. Burke, C. Koh, T. Vallet, J.A. Silvas, C.M. Azumaya, C. Billesbolle, A.F. Brilot, M.G. Campbell, A. Diallo, M.S. Dickinson, D. Diwanji, N. Herrera, N. Hoppe, H.T. Kratochvil, Y. Liu, G.E. Merz, M. Moritz, H. C. Nguyen, C. Nowotny, C. Puchades, A.N. Rizo, U. Schulze-Gahmen, A.M. Smith, M. Sun, I.D. Young, J. Zhao, D. Asarnow, J. Biel, A. Bowen, J.R. Braxton, J. Chen, C.M. Chio, U.S. Chio, I. Deshpande, L. Doan, B. Faust, S. Flores, M. Jin, K. Kim, V.L. Lam, F. Li, J. Li, Y.L. Li, Y. Li, X. Liu, M. Lo, K.E. Lopez, A.A. Melo, F. R. Moss 3rd, P. Nguyen, J. Paulino, K.I. Pawar, J.K. Peters, T.H. Pospiech Jr., M. Safari, S. Sangwan, K. Schaefer, P.V. Thomas, A.C. Thwin, R. Trenker, E. Tse, T. K.M. Tsui, F. Wang, N. Whitis, Z. Yu, K. Zhang, Y. Zhang, F. Zhou, D. Saltzberg, Q.S.B. Consortium, A.J. Hodder, A.S. Shun-Shion, D.M. Williams, K.M. White, R. Rosales, T. Kehrer, L. Miorin, E. Moreno, A.H. Patel, S. Rihn, M.M. Khalid, A. Vallejo-Gracia, P. Fozouni, C.R. Simoneau, T.L. Roth, D. Wu, M.A. Karim, M. Ghoussaini, I. Dunham, F. Berardi, S. Weigang, M. Chazal, J. Park, J. Logue, M. McGrath, S. Weston, R. Haupt, C.J. Hastie, M. Elliott, F. Brown, K.A. Burness, E. Reid, M. Dorward, C. Johnson, S.G. Wilkinson, A. Geyer, D.M. Giesel, C. Baillie, S. Raggett, H. Leech, R. Toth, N. Goodman, K.C. Keough, A.L. Lind, C. Zoonomia, R.J. Klesh, K.R. Hemphill, J. Carlson-Stevermer, J. Oki, K. Holden, T. Maures, K.S. Pollard, A. Sali, D.A. Agard, Y. Cheng, J.S. Fraser, A. Frost, N. Jura, T. Kortemme, A. Manglik, D.R. Southworth, R.M. Stroud, D.R. Alessi, P. Davies, M.B. Frieman, T. Ideker, C. Abate, N. Jouvenet, G. Kochs, B. Shoichet, M. Ott, M. Palmarini, K.M. Shokat, A. Garcia-Sastre, J.A. Rassen, R. Grosse, O.S. Rosenberg, K.A. Verba, C.F. Basler, M. Vignuzzi, A.A. Peden, P. Beltrao, N. J. Krogan, Comparative host-coronavirus protein interaction networks reveal pan-viral disease mechanisms, Science 370 (2020), https://doi.org/10.1126/science.abe9403.
[74] C.R. Choi, H.W. Rhee, Proximity labeling: an enzymatic tool for spatial biology, Trends Biotechnol. 40 (2022) 145–148, https://doi.org/10.1016/j.tibtech.2021.09.008.
[75] M.G. Kang, H.W. Rhee, Molecular spatiomics by proximity labeling, Acc. Chem. Res. 55 (2022) 1411–1422, https://doi.org/10.1021/acs.accounts.2c00061.